nature cell biology

ARTICLES

https://doi.org/10.1038/s41556-022-00850-x

Check for updates

EZH2 noncanonically binds cMyc and p300 through a cryptic transactivation domain to mediate gene activation and promote oncogenesis

Jun Wang[1,2,8], Xufen Yu[3,8], Weida Gong[1], Xijuan Liu[1], Kwang-Su Park[3], Anqi Ma[3], Yi-Hsuan Tsai[1], Yudao Shen[3], Takashi Onikubo[4], Wen-Chieh Pi[5], David F. Allison[1,2], Jing Liu[3], Wei-Yi Chen[5], Ling Cai[1,6], Robert G. Roeder[4], Jian Jin[3] ✉ and Gang Greg Wang[1,2,7] ✉

Canonically, EZH2 serves as the catalytic subunit of PRC2, which mediates H3K27me3 deposition and transcriptional repression. Here, we report that in acute leukaemias, EZH2 has additional noncanonical functions by binding cMyc at non-PRC2 targets and uses a hidden transactivation domain (TAD) for (co)activator recruitment and gene activation. Both canonical (EZH2–PRC2) and noncanonical (EZH2-TAD–cMyc–coactivators) activities of EZH2 promote oncogenesis, which explains the slow and ineffective antitumour effect of inhibitors of the catalytic function of EZH2. To suppress the multifaceted activities of EZH2, we used proteolysis-targeting chimera (PROTAC) to develop a degrader, MS177, which achieved effective, on-target depletion of EZH2 and interacting partners (that is, both canonical EZH2–PRC2 and noncanonical EZH2–cMyc complexes). Compared with inhibitors of the enzymatic function of EZH2, MS177 is fast-acting and more potent in suppressing cancer growth. This study reveals noncanonical oncogenic roles of EZH2, reports a PROTAC for targeting the multifaceted tumorigenic functions of EZH2 and presents an attractive strategy for treating EZH2-dependent cancers.

The canonical function of Enhancer of zeste homologue 2 (EZH2) is to serve as the enzymatic subunit of Polycomb repressive complex 2 (PRC2), which catalyses histone H3 lysine 27 trimethylation (H3K27me3) to maintain a gene-repressive chromatin state[1,2]. EZH2 overexpression is associated with cancer progression and poor outcomes in patients[3–6]. Exquisite EZH2 dependencies have been demonstrated in various cancers[4,6–10]; therefore, targeting EZH2 represents an attractive anticancer strategy.

Inhibitors that target the su(var)3–9, enhancer-of-zeste and trithorax (SET) domain of EZH2 have been developed[11], such as EPZ-6438 (refs. [12,13]), GSK126 (ref. [14]), UNC1999 (ref. [15]), C24 (ref. [16]) and CPI-1205 (ref. [17]). However, these inhibitors often exerted slow and/or partial cellular responses[18,19] (see below), which probably stems from the failure to target the noncatalytic functions of EZH2. Besides PRC2, EZH2 can recruit or bind non-PRC2 factors to modulate gene expression during oncogenesis[10,20]. PRC2-independent functions of EZH2 have been associated with transcriptional activation rather than H3K27me3-related repression, as exemplified by the interaction of EZH2 with non-PRC2 partners, including the androgen receptor and NF-κB in prostate cancer[10] and breast cancer[21–23], respectively. Notably, non-PRC2-related activities of EZH2 are often methyltransferase-independent[10,20,23–27]. Thus, current EZH2 inhibitors, which only inhibit the catalytic activity of EZH2 (catalytic inhibitors), may fail to suppress its noncanonical activities.

Our studies of *MLL1*-rearranged (MLL-r) leukaemia, a genetically defined blood malignancy that has poor prognosis[28,29], have revealed that besides canonical EZH2–PRC2-bound targets, EZH2 has noncanonical targets that lack H3K27me3 but contain the gene-activation-related markers, including histone acetylation, RNA polymerase II (Pol II) and coactivators. At noncanonical targets, EZH2 directly binds cMyc and a coactivator (p300) via a cryptic TAD, which mediates gene activation and contributes to oncogenesis. Consequently, enzymatic inhibitors of EZH2 are generally ineffective in treating MLL-r leukaemias. To develop a strategy that suppresses the multifaceted functions of EZH2, we used PROTAC technology[30–33] and developed MS177, an EZH2-targeting PROTAC degrader. Biochemical, cellular, genomic and animal studies demonstrate that MS177 effectively depletes both canonical EZH2–PRC2 and noncanonical EZH2–cMyc complexes and that MS177 is more effective and fast-acting than catalytic inhibitors of EZH2 in killing tumours.

Results

EZH2 noncanonically binds sites with gene-active markers. To systematically define gene-regulatory roles for EZH2 in MLL-r leukaemia, we performed chromatin immunoprecipitation with sequencing (ChIP-seq) for EZH2 and H3K27me3, an enzymatic product characteristic of EZH2–PRC2, in two independent leukaemia cell lines with MLL-r: EOL-1 (which harbours a MLL partial tandem duplication) and MV4;11 (which harbours MLL-AF4 fusion). A large majority of EZH2 peaks overlapped with H3K27me3, which specify canonical EZH2–PRC2 sites (Extended

[1]Lineberger Comprehensive Cancer Center, University of North Carolina at Chapel Hill School of Medicine, Chapel Hill, NC, USA. [2]Department of Biochemistry and Biophysics, University of North Carolina at Chapel Hill School of Medicine, Chapel Hill, NC, USA. [3]Mount Sinai Center for Therapeutics Discovery, Departments of Pharmacological Sciences and Oncological Sciences, Tisch Cancer Institute, Icahn School of Medicine at Mount Sinai, New York, NY, USA. [4]Laboratory of Biochemistry and Molecular Biology, The Rockefeller University, New York, USA. [5]Institute of Biochemistry and Molecular Biology, National Yang Ming Chiao Tung University, Taipei, Taiwan. [6]Department of Genetics, University of North Carolina at Chapel Hill School of Medicine, Chapel Hill, NC, USA. [7]Department of Pharmacology, University of North Carolina at Chapel Hill School of Medicine, Chapel Hill, NC, USA. [8]These authors contributed equally: Jun Wang, Xufen Yu. ✉e-mail: jian.jin@mssm.edu; greg_wang@med.unc.edu

Data Fig. 1a–d). Meanwhile, a subset of EZH2 sites lacked H3K27me3 (29% and 32% in EOL-1 and MV4;11 cells, respectively), termed as EZH2-'solo'-binding sites (Extended Data Fig. 1a–d). Interrogation of additional chromatin marks showed that EZH2-solo-binding peaks were overwhelmingly enriched for the gene-activation-related H3K4me3, H3K27ac and H3K9ac peaks, which is in contrast to what was seen with the EZH2–H3K27me3 cobound peaks (Fig. 1a–d). To rule out potential artifacts, we used a second profiling method, cleavage under targets and release using nuclease (CUT&RUN)[34], and cells stably expressing haemagglutinin (HA)-tagged EZH2. CUT&RUN for HA–EZH2 in both EOL-1 and MV4;11 cells verified noncanonical and canonical EZH2 sites (Fig. 1a–d; HA–EZH2). EZH2-solo-binding sites identified from these two leukaemia cell lines showed significant overlap (Fig. 1e), which indicates that there is a conserved mechanism underlying EZH2-solo-binding formation. EZH2-solo peaks also exhibited significant colocalization with Pol II, MLL (a writer of H3K4me3), BRD4 (a reader of histone acetylation) and SWI/SNF complexes (Fig. 1f–i), which again indicates a role for gene activation for these sites. Thus, EZH2-solo-targeting sites exist in MLL-r leukaemias and are potentially involved in transcriptional activation, which differ from the canonical roles of EZH2–PRC2 for H3K27me3 deposition and gene repression.

EZH2-solo sites are bound by oncoproteins, notably cMyc. A motif search analysis using EZH2-solo peaks revealed enrichment for consensus binding sites of the basic helix–loop–helix (bHLH) transcription factor (TF), such as CACGTG (a canonical cMyc site) and CAGCTG (a non-cMyc bHLH TF site), and motifs of the ETS family of TFs (Fig. 1j and Extended Data Fig. 1e). Previous studies have shown that cMyc-binding sites do not correlate well with the presence of high-affinity cMyc motifs[35–39] and that low-affinity motifs, including CAGCTG, are enriched at cMyc-binding sites, which highlights the complexity of these recruitment mechanisms[35]. Moreover, cMyc is colocalized with basal transcription apparatus and/or chromatin-modulatory proteins such as Pol II, P-TEFb, NuA4, TRRAP, SWI/SNF and WDR5–MLL complexes, due to direct or indirect interactions[36,38–44]. As same sets of (co)activators were enriched at EZH2-solo sites in leukaemia cells, we therefore tested biochemical association among EZH2, cMyc and (co)activators.

First, co-immunoprecipitation (co-IP) assays detected interactions of EZH2 with p300, SWI/SNF and Pol II, similar to what was observed for cMyc (Fig. 1k,l and Extended Data Fig. 1f). Additionally, EZH2, expressed endogenously or exogenously, interacted with cMyc–MAX (Fig. 1m,n and Extended Data Fig. 1g–j), and this association was intact under cell treatment with Benzonase and ethidium bromide (Extended Data Fig. 1g), which indicates that this interaction does not depend on DNA. Recombinant EZH2 also efficiently bound to cMyc (Fig. 1o). Interestingly, EZH2 bound both PRC2 subunits and cMyc–MAX (Fig. 1m), whereas cMyc–MAX interacted with EZH2 only, and not other PRC2 components, in co-IP and glutathione *S*-transferase (GST) pulldown assays (Fig. 1n–p). These observations suggest that the EZH2 association with cMyc is PRC2-independent and occurs at EZH2-solo-binding sites.

Next, we performed CUT&RUN for cMyc in EOL-1 and MV4;11 cells using independent anti-cMyc antibodies, which produced highly correlated results (Extended Data Fig. 1k). Indeed, significant colocalization of cMyc was seen at the EZH2-solo-binding sites but not EZH2–H3K27me3 cobound PRC2 peaks (Fig. 1q,r). About 50% of the EZH2–cMyc cobound peaks were located at promoters (Extended Data Fig. 1l), which is consistent with the association of cMyc with basal transcription apparatus and (co)activators[36,38–44]. To further verify our finding in a model that closely resembles the clinical setting, we conducted CUT&RUN with patient-derived xenograft (PDX) cells from patients with acute myeloid leukaemia (AML) who harbour MLL-AF9 fusion gene. We found similar EZH2–cMyc co-binding at those EZH2-solo sites identified from MV4;11 cells, which are again featured with high H3K27ac and no or low H3K27me3 (Fig. 1s, top). Meanwhile, and as expected, those canonical EZH2–PRC2-bound sites identified from MV4;11 cells exhibited high H3K27me3 and no or low H3K27ac in PDX cells (Fig. 1s, bottom).

Collectively, co-targeting of EZH2 and cMyc onto noncanonical EZH2 sites exists among independent MLL-r leukaemia models. Interestingly, additional analyses using public datasets of three healthy or non-AML cell types (that is, GM12878 lymphoblasts, human umbilical vein endothelial cells (HUVECs) and K562 cells) showed an overwhelming pattern of EZH2–H3K27me3 colocalization and a lack of EZH2-solo–cMyc co-binding (Extended Data Fig. 1m). These results indicate that the EZH2–cMyc association seen at noncanonical EZH2 sites in MLL-r leukaemias is probably associated with malignant transformation, which merits further investigation.

The EZH2 TAD directly interacts with cMyc and (co)activators. To dissect the gene-regulatory roles of EZH2 and cMyc in MLL-r leukaemias, we conducted RNA sequencing (RNA-seq) following their depletion. As expected, depletion of either EZH2 or cMyc significantly suppressed leukaemia cell growth (Extended Data Fig. 2a–d). Differentially expressed genes (DEGs) that showed downregulation after EZH2 or cMyc depletion displayed partial but significant overlap (~21–25%, $P < 5.8 \times 10^{-92}$; Fig. 2a and Supplementary Table 1). EZH2 and cMyc co-upregulated genes exhibited co-binding of EZH2, cMyc, H3K27ac and H3K9ac while lacking H3K27me3 (Fig. 2b), which is consistent with the gene-activation roles of EZH2

Fig. 1 | EZH2 exhibits noncanonical PRC2-independent solo-binding in leukaemias. Besides its canonical H3K27me3 cobound pattern, EZH2 exhibits additional noncanonical solo-binding at sites enriched for gene-activation-related histone marks, Pol II, (co)activators and cMyc in MLL-r leukaemia cells. **a**–**d**, Averaged signal intensities (**a**,**b**) and heatmaps (**c**,**d**) for EZH2 (either endogenous EZH2 or exogenously expressed HA-tagged EZH2), H3K27me3, histone acetylation (H3K27ac or H3K9ac) and H3K4me3 ±5 kb from the centres of noncanonical EZH2^{+}H3K27me3^{-} peaks (that is, EZH2-solo; top) or canonical EZH2^{+}H3K27me3^{+} peaks (that is, EZH2 ensemble; bottom) in either MV4;11 (**a**,**c**) or EOL-1 (**b**,**d**) cells. With the exception of HA–EZH2, which was mapped using CUT&RUN, all the others were mapped using ChIP-seq. **e**, Venn diagram showing the significant overlap between EZH2-solo-binding sites identified in the two independent MLL-r leukaemia cell lines MV4;11 and EOL-1. **f**–**i**, Heatmaps of ChIP-seq signals for EZH2 and Pol II (**f**), MLL (MLLn and MLLc; **g**), BRD4 (**h**), and SWI/SNF (SMARCA4 and SMARCC1; **i**) ±5 kb from the centres of EZH2-solo-binding sites in MV4;11 or EOL-1 cells. **j**, Significant enrichment of the Myc:MAX motif (CACGTG) at the EZH2-solo peaks in MV4;11 cells. **k**,**l**, Co-IP for EZH2 (**k**) or cMyc (**l**) interactions with endogenous Pol II, SMARCA4 and SMARCB1 in EOL-1 cells using anti-EZH2 or anti-cMyc antibodies. **m**,**n**, Co-IP for endogenous EZH2 and cMyc interactions in EOL-1 cells using anti-EZH2 (**m**) or anti-cMyc (**n**) antibodies. Classic PRC2 subunits, SUZ12 and EED, and MAX, the cMyc cofactor, were probed in IP samples. **o**,**p**, GST pulldown for assaying interactions of the in vitro translated (IVT) HA–cMyc protein with recombinant GST–EZH2 (**o**) or GST–EED (**p**) protein. GST alone (lane 1) served as the control. Red arrows indicate GST and GST-fusion protein. **q**,**r**, Averaged ChIP-seq signal intensities (**q**) and heatmaps (**r**) for EZH2 and cMyc (using two independent antibodies, ab1 and ab2) ±5 kb from the centres of noncanonical EZH2-solo peaks (left) or canonical EZH2 ensemble peaks (right) in MV4;11 (top) or EOL-1 (bottom) cells. **s**, Heatmaps for EZH2, H3K27me3, cMyc and H3K27ac signal intensities, detected by CUT&RUN, in MLL-AF9^{+} AML PDX cells, ±5 kb from the centres of either EZH2-solo (top) or EZH2 ensemble (bottom) sites identified in MLL-AF4^{+} MV4;11 cells.

and cMyc at these targets. Gene Ontology (GO) analysis showed that the EZH2–cMyc co-regulated transcripts were enriched for genes related to cell metabolism and leukaemia or lymphoma oncogenesis (Fig. 2c). RNA-seq analyses with or without the spike-in control normalization generated consistent results (Extended Data Fig. 2e–i). EZH2-solo-bound genes were generally expressed at a level higher than EZH2–PRC2-targeted genes (Extended Data Fig. 2j,k). By integrating genome-binding and RNA-seq datasets, we further identified the EZH2–cMyc co-regulated genes that are directly cobound by EZH2-solo and cMyc (Fig. 2d and Extended Data Fig. 2l), such as *TPD52*, *IRF2BPL*, *GADD45B*, *CD55* and *ADAM9*, which exhibited co-binding of Pol II and gene-active

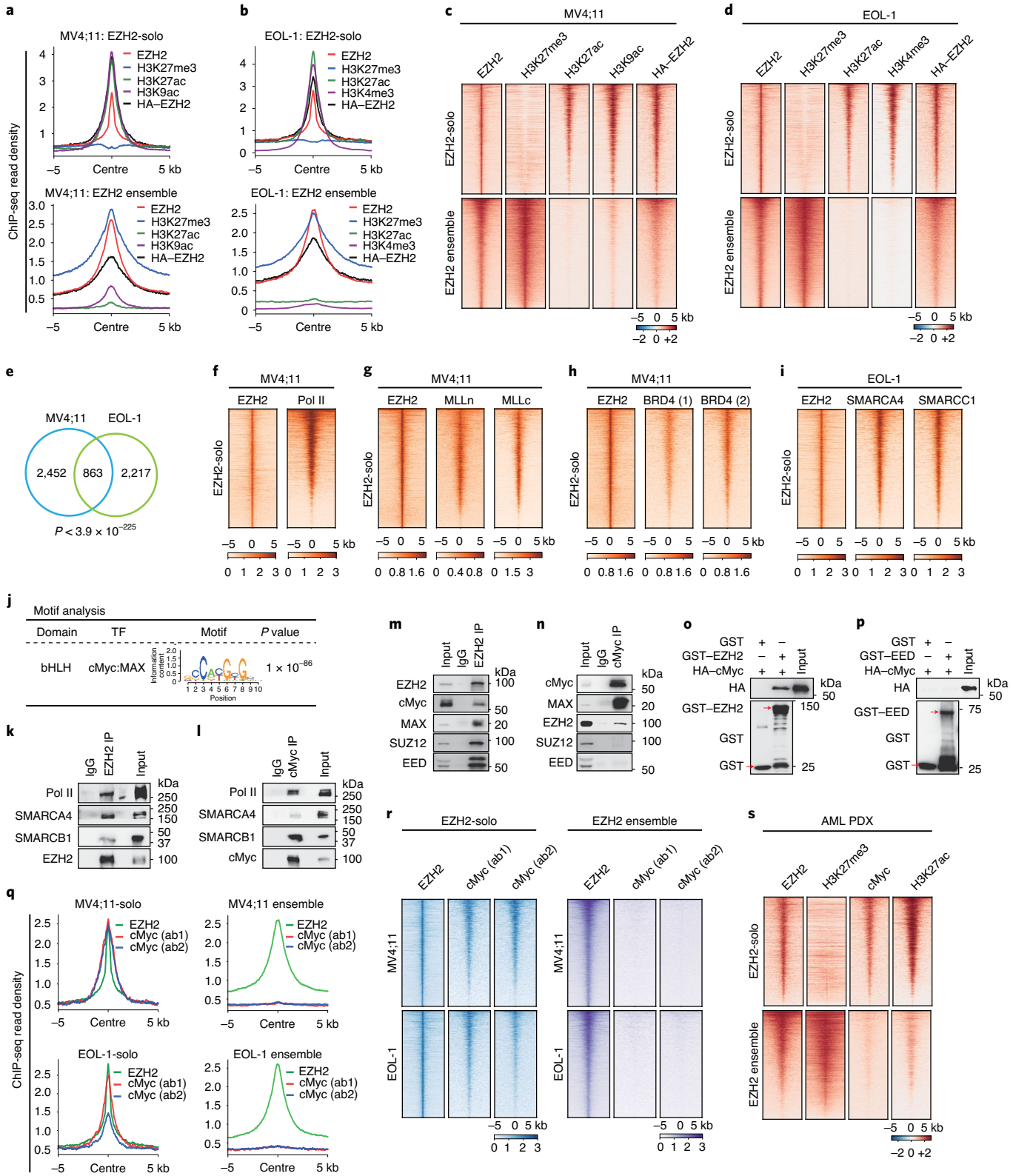

markers (H3K27ac, H3K9ac and H3K4me3) but lacked H3K27me3 (Fig. 2e,f and Extended Data Fig. 2m). Higher expression of *TPD52* or *IRF2BPL* was correlated with poorer prognosis in patients with AML (Fig. 2g,h). PCR with reverse transcription (RT–PCR) analysis further showed that the expression of selected genes that exhibit EZH2-solo and cMyc co-binding are dependent on both EZH2 and cMyc. These genes were largely insensitive to PRC2 blockade, as shown by treatment with C24 (an EZH2 enzymatic inhibitor that erases global H3K27me3)[16] or UNC6852 (an EED PROTAC that degrades PRC2)[45], but were significantly inhibited after treatment with A-485 (a p300/CBP inhibitor)[46] (Fig. 2i,j and Extended Data Fig. 2n,p). These results therefore confirm that EZH2 and its interacting coactivators have a PRC2-independent gene-activation role. Meanwhile, cMyc depletion led to a concurrently decreased binding of cMyc and EZH2 to their co-targeted sites; conversely, EZH2 depletion decreased both EZH2 and cMyc recruitment onto these same sites (Fig. 2k,l and Extended Data Fig. 2c,q). These results indicate that there is cooperative recruitment of EZH2 and cMyc for target gene activation.

To dissect the mechanism that underlies EZH2-mediated transactivation, we analysed its protein sequence with 9aaTAD[47], a tool for predicting the TAD. Consistent with a previous report[48], putative TADs were identified within amino acids 135–200 of EZH2, which comprises two typical, partially disordered Φ-Φ-x-x-Φ motifs (with Φ representing a hydrophobic residue and x being any residue; Fig. 3a and Extended Data Fig. 3a,b). In luciferase reporter assays, EZH2-TAD and VP16-TAD displayed comparable transactivation capabilities (Fig. 3b and Extended Data Fig. 3c). Substitution of Phe145 or Phe171 in EZH2-TAD with alanine or lysine greatly reduced TAD-mediated transactivation, with the dual mutants exhibiting close to complete abolishment (Fig. 3c). In support of a role for EZH2-TAD in gene activation, GST pulldown using recombinant EZH2-TAD protein readily detected interactions with cMyc, p300 and SWI/SNF complexes (Fig. 3d), which is in agreement with their co-occupancies at EZH2-solo-binding sites. Meanwhile, EZH2-TAD-dead mutations almost completely abrogated EZH2-TAD interactions with cMyc, p300 and SWI/SNF (Fig. 3e). Next, we mapped the EZH2-interaction interface of cMyc to its central domain (cMyc-CD; Fig. 3f). Isothermal titration calorimetry (ITC) further confirmed a direct binding between EZH2-TAD and cMyc-CD, with the dissociation constant (K_d) measured as ~1.5 μM, whereas the EZH2-TAD-dead mutant showed no detectable interaction with cMyc-CD (Fig. 3g,h). GST pulldown also verified the EZH2-TAD interaction with recombinant p300 (Fig. 3i).

Collectively, EZH2-TAD forms direct interactions with (co) activators, including cMyc and p300, which underlies their cooperation in the chromatin recruitment and gene activation seen at EZH2-solo targets, some of which are the clinically relevant genes such as *TPD52* and *IRF2BPL*.

EZH2-TAD is required for malignant growth of leukaemia cells. Next, we assessed the requirement of EZH2-TAD for malignant growth. First, co-IP showed that cMyc associated with wild-type full-length EZH2 but not its TAD-dead mutant (Fig. 3j), which indicates that EZH2-TAD is essential for cMyc interactions in cells. Genetic complementation using MV4;11 cells in which endogenous EZH2 was depleted demonstrated that wild-type but not TAD-dead EZH2 rescued the growth defect (Fig. 3k,l). Compared to the wild type, the TAD-dead EZH2 also exhibited defects in gene activation and binding to the EZH2-solo targets (Fig. 3m,n). Thus, EZH2–cMyc:(co)activator-complex-mediated activation of noncanonical EZH2 targets is crucial for malignant growth in MLL-r AML.

Development of the EZH2-targeting PROTAC degrader MS177. EZH2 is essential for oncogenesis of MLL-r leukaemias[8,9,49]. However, C24 (Fig. 4a, left), a potent enzymatic inhibitor of EZH2 with a half maximal inhibitory concentration (IC_{50}) of 12 nM (ref. [16]), had little to very mild growth-suppressive effects on a panel of MLL-r leukaemia cell lines (Extended Data Fig. 4a). Such a poor tumour-killing effect is probably due to the failure of C24 to target the noncanonical functions of EZH2, such as EZH2–cMyc-mediated activation of nonconventional targets, which we showed to be TAD-dependent and PRC2-independent.

A different strategy is needed to target both the canonical and noncanonical tumorigenic activities of EZH2, and we used the PROTAC technology. The piperazine moiety of C24 is solvent-exposed, which presents a handle for connecting an E3 ligase ligand without interfering with EZH2 binding[16,50]. Testing of various putative EZH2 PROTAC degraders led to the identification of MS177, an effective EZH2-targeting PROTAC, which consists of pomalidomide, a CRBN ligand[51], conjugated to C24 via a short polyethylene glycol linker (Fig. 4a). We also designed and synthesized two structurally similar analogues of MS177 as controls: MS177N1 and MS177N2 (Fig. 4a). MS177N1 has a methyl group added to the glutarimide moiety of pomalidomide, and was designed to disrupt CRBN binding while maintaining EZH2 binding[52]. MS177N2 has two methyl groups added to the C24 portion of MS177, and was designed to abolish EZH2 binding without affecting CRBN binding[15,16,50]. Thus, MS177, but not MS177N1 or MS177N2, would induce EZH2 degradation (Extended data Fig. 5a). First, we showed that C24, MS177 and MS177N1 all displayed comparable high potencies to inhibit EZH2–PRC2 in vitro, whereas MS177N2 did not exhibit significant inhibition (Fig. 4b). Similar to C24, MS177 retained high selectivity for EZH2 over EZH1 and other unrelated methyltransferases

Fig. 2 | Cooperative EZH2 and cMyc recruitment to common targets leads to gene activation in leukaemia. a, Venn diagram using DEGs, downregulated based on RNA-seq analysis after *EZH2* knockdown (KD; shEZH2) or *cMyc* KO (either sgcMyc-1 or sgcMyc-5) in MV4;11 cells ($n = 2$ biologically independent experiments). The threshold of DEGs is set as adjusted DESeq *P* value (q) < 0.05, fold-change (FC) > 1.25 and mean tag counts > 10. |FC| indicates the absolute value of FC. **b**, Averaged signal intensities of EZH2 (endogenous EZH2 or exogenously expressed HA-EZH2), cMyc, H3K27ac, H3K9ac and H3K27me3 around the genes co-upregulated by EZH2 and cMyc in MV4;11 cells ($n = 204$ common regulated genes; defined in **a**). TES, transcriptional end site; TSS, transcriptional start site. **c**, GO analysis (top) and enrichment of the DisGeNET category (bottom) using genes co-upregulated by EZH2 and cMyc shown in **a**. **d**, Heatmap using the indicated RNA-seq sample comparison shows $\log_2$-converted ratios of the 204 genes co-upregulated by EZH2 and cMyc in MV4;11 cells ($n = 2$ biologically independent experiments). Genes with the EZH2-solo-cMyc co-binding are labelled. EV, empty vector. **e**,**f**, Integrative Genomics Viewer (IGV) image of enrichment for the indicated factor at *TPD52* (**e**) and *IRF2BPL* (**f**) in MV4;11 cells. **g**,**h**, Kaplan–Meier overall survival analysis based on the *TPD52* (**g**) or *IRF2BPL* (**h**) expression in patient samples from the AML cohort of The Caner Genomics Atlas. Statistical significance was determined by log-rank test. **i**,**j**, RT-qPCR for the indicated EZH2–cMyc co-targeted genes following *EZH2* KD or *cMyc* KO (**i**), or after a 24-h treatment with 2.5 μM of UNC6852, C24 or A-485 (**j**), in MV4;11 cells. The *y* axis shows averaged signals after normalization to GAPDH and to mock-treated ($n = 3$; mean ± s.d.; unpaired two-tailed Student's *t*-test). **k**,**l**, ChIP-qPCR for cMyc and EZH2 at the indicated EZH2–cMyc co-targeted gene promoter in MV4;11 cells after depletion of cMyc (**k**) or EZH2 (**l**). The *y* axis shows averaged signals after normalization to input and then to EV controls ($n = 3$; mean ± s.d.; unpaired two-tailed Student's *t*-test). $^*P < 0.05$, $^{**}P < 0.01$, $^{***}P < 0.005$. NS, not significant. Numerical source data, statistics and exact *P* values are available as source data.

(Extended Data Fig. 5b,c), and a panel of common drug targets, including kinases, G protein-coupled receptors (GPCRs), ion channels and transporters (Supplementary Tables 2 and 3). In HeLa cells, C24, MS177 and MS177N1, but not MS177N2, also inhibited the enzymatic activities of EZH2–PRC2, decreased H3K27me3 and increased H3K27ac without affecting other tested histone modifications (Extended Data Fig. 5d and Fig. 4c). Collectively, MS177 is a potent and selective EZH2-targeting compound.

MS177 effectively degrades cellular EZH2–PRC2. We next assessed the capacity of MS177 to degrade EZH2 in cells. First, we observed that in multiple MLL-r leukaemia cell lines, MS177 depleted EZH2, EED and SUZ12 in a concentration- and time-dependent fashion, an effect not seen with C24, MS177N1 or MS177N2 (Fig. 4d–g and Extended Data Fig. 5e,f). Cellular EZH2 levels were restored 24 h after washout of MS177 (Fig. 4h). As expected, treatment with MS177, MS177N1 or C24,

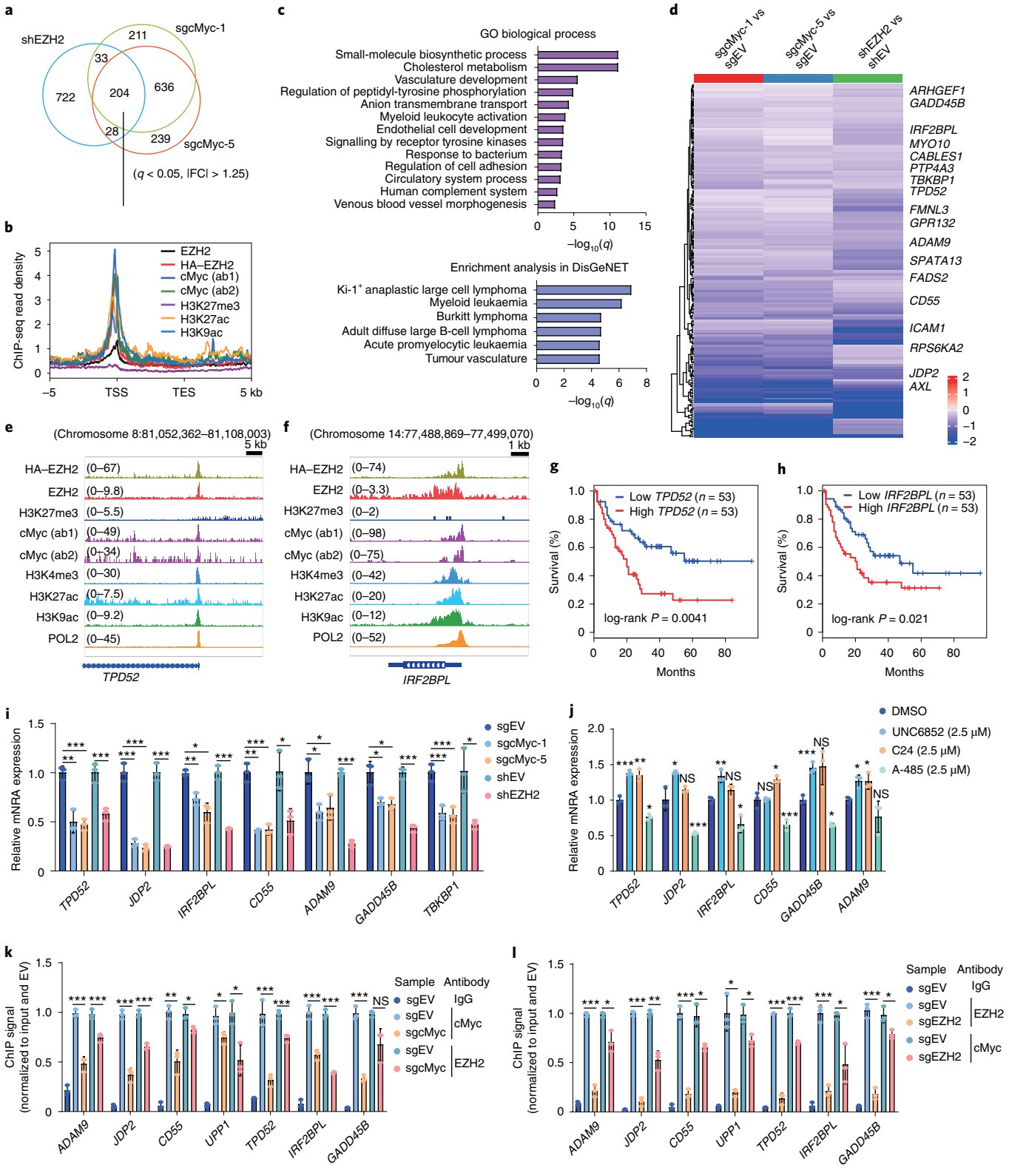

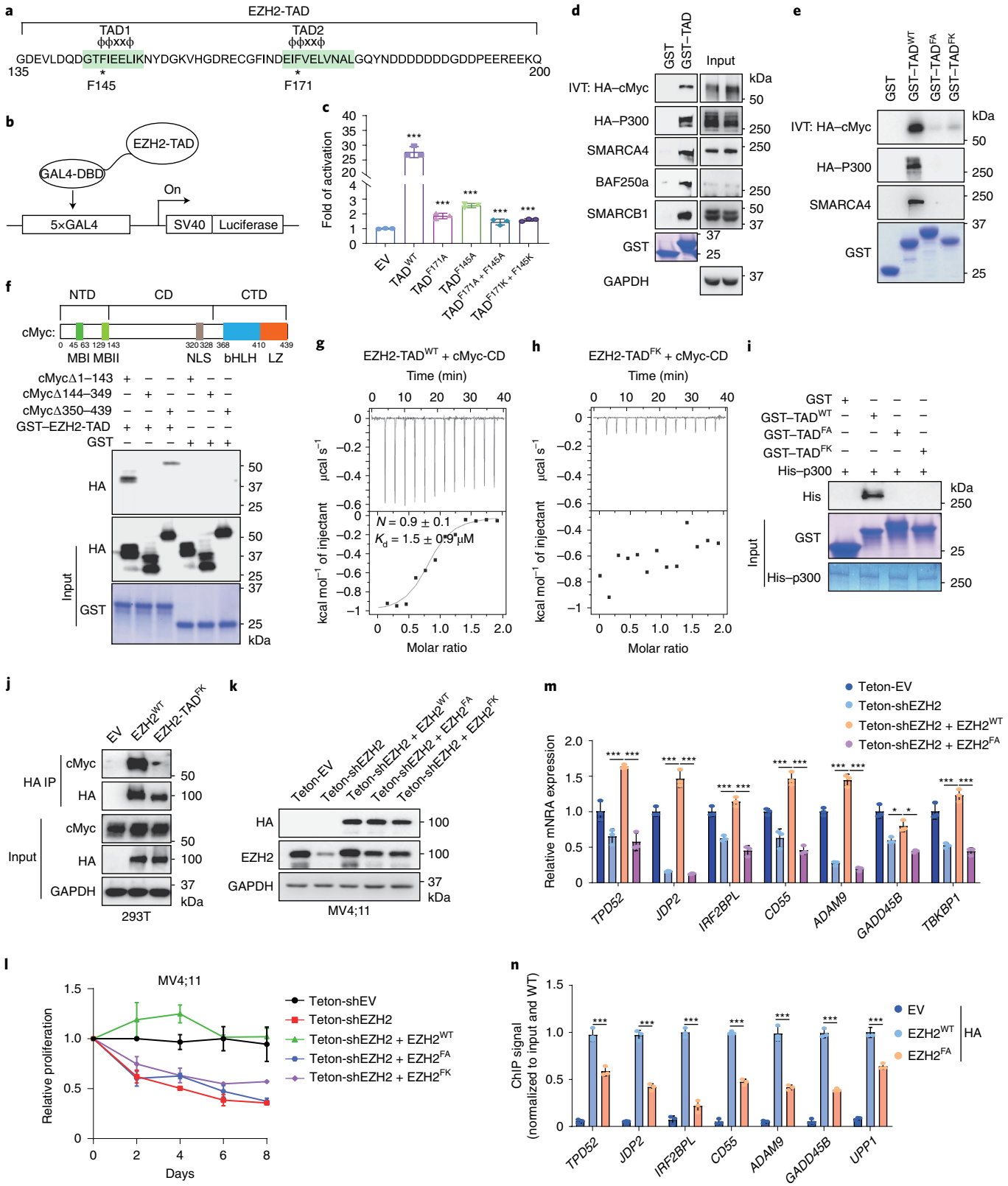

but not MS177N2, suppressed global H3K27me3 in leukaemia cells (Fig. 4d,f and Extended Data Fig. 5e). In EOL-1 and MV4;11 cells, MS177 exhibited half-maximal degradation concentration (DC_{50}) values of 0.2 ± 0.1 μM and 1.5 ± 0.2 μM, and maximum degradation (D_{max}) values of 82% and 68%, respectively (Fig. 4e and Extended Data Fig. 5g).

We next assessed the mechanism of action (MOA) of MS177 to degrade EZH2. First, co-IP showed that neither C24 nor MS177N1 treatment interfered with the PRC2–EZH2 or EZH2–cMyc interactions (Fig. 4i). In agreement with MS177 being a PROTAC, cellular EZH2 was ubiquitinated after treatment with MS177, but not C24 (Fig. 4j). Pretreatment of cells with C24 attenuated

Fig. 3 | EZH2 directly interacts with cMyc and coactivators via EZH2-TAD to promote malignant growth of leukaemia cells. a, EZH2-TAD, highlighted in green, contains typical Φ-Φ-x-x-Φ motifs, with asterisks indicating aromatic residues that are important for transactivation. **b**,**c**, Schematic of GAL4-based luciferase reporter assays (**b**) and summary (**c**) of reporter activities of EZH2-TAD, either wild type (WT) or mutant, compared to EV. The *y* axis shows relative activation after normalization to internal control (Renilla luciferase) and then to EV-transduced mock ($n=3$; mean ± s.d.; unpaired two-tailed Student's *t*-test). DBD, DNA-binding domain. **d**,**e**, Pulldown using GST alone or GST–EZH2-TAD, either WT (**d**) or TAD-dead-mutant (**e**), and the IVT protein of HA–cMyc or 293T cell lysate containing the transiently expressed HA–p300. FA, F145A+F171A; FK, F145K+F171K. **f**, Schematic of the domain organization of cMyc (top) and pulldown (bottom) using GST alone or GST–EZH2-TAD and 293T cell lysate containing the transiently expressed HA–cMyc with serial truncation. NTD, CD and CTD indicate the amino-terminal, central and carboxy-terminal domains, respectively. **g**,**h**, ITC binding curves using recombinant EZH2-TAD, either WT (**g**) or TAD-dead-mutant (**h**), and purified cMyc-CD ($n=3$; mean ± s.d.). **i**, Pulldown using GST–EZH2-TAD, WT or mutant, and recombinant His6×-p300 (His–p300) protein. **j**, Co-IP for endogenous cMyc and the stably expressed full-length HA–EZH2, either WT or TAD-dead-mutant, in 293T cells. **k**–**m**, Immunoblot of the indicated protein (**k**), cell proliferation (**l**) and RT–qPCR of EZH2–cMyc-coactivated genes (**m**) after doxycycline-induced depletion of endogenous EZH2 in MV4;11 cells, pre-rescued with exogenous shEZH2-resistant HA–EZH2, either WT or TAD-dead-mutant (FA or FK). Teton, doxycycline (dox)-inducible Tet-On vector. For **l** and **m**, $n=3$, mean ± s.d.; for **m**, unpaired two-tailed Student's *t*-test was used. **n**, ChIP–qPCR of HA–EZH2, either WT or TAD-dead-mutant, at the indicated EZH2–cMyc co-targeted gene using the same MV4;11 cells shown in **k**–**m**. The *y* axis shows signals after normalization to those from input and then to WT HA–EZH2-transduced cells ($n=3$; mean ± s.d.; unpaired two-tailed Student's *t*-test). EV-transduced cells served as the negative control. $^{*}P<0.05$, $^{**}P<0.01$ and $^{***}P<0.005$. Numerical source data, statistics, exact *P* values and unprocessed blots are available as source data.

the MS177-induced PRC2–EZH2 depletion (Fig. 4k,l). Also, the MS177-induced EZH2 degradation effect was effectively blocked by pretreatment with the CRBN ligand pomalidomide (Fig. 4m) or MLN4924 (which suppresses the assembly of Cullin-based E3 ligase[53]; Fig. 4n). Last, *CRBN* knockout (KO) also almost completely abrogated MS177-induced EZH2 depletion (Fig. 4o). Thus, MS177 is a bone fide CRBN-dependent, EZH2-targeting PROTAC that effectively degrades EZH2 and associated PRC2 in cells.

MS177 efficiently suppresses EZH2–PRC2 functions in cells. MS177 exhibited comparable depletion effect on both nucleoplasmic and chromatin-bound EZH2 (Extended Data Fig. 6a). We next performed ChIP-seq for EZH2 and H3K27me3 after treatment of leukaemia cells with MS177 and C24 (Supplementary Table 4). This revealed that relative to mock treatment, MS177, but not C24, decreased overall levels of chromatin-bound EZH2, whereas both compounds suppressed global H3K27me3 (Fig. 5a–d), as exemplified by what was observed at canonical EZH2–PRC2 targets (Fig. 5e,f and Extended Data Fig. 6b). Thus, compared to C24, MS177 reduces chromatin-bound EZH2, which highlights a potential advantage of the EZH2-targeting PROTAC degrader over inhibitors of the enzymatic function of EZH2.

We then conducted RNA-seq after treatment of three independent MLL-r leukaemia models with MS177, C24 or MS177N1. Despite background differences, leukaemia cells treated with MS177 displayed a greater similarity among the cell lines than those treated with C24 or MS177N1 (Extended Data Fig. 6c). Moreover, DEGs caused by MS177 treatment overlapped significantly among independent leukaemia models (Fig. 5g). Notably, robust transcriptomic changes were observed after treatment with MS177, but not C24 or MS177N1, relative to mock (Supplementary Tables 5 and 6). A significant proportion of DEGs were directly bound by EZH2 (Extended Data Fig. 6d). Moreover, those DEGs de-repressed by MS177 showed little to mild de-repression after comparable treatment with C24 or MS177N1 (Fig. 5h–j).

We next aimed to further assess the effect of MS177 canonical EZH2–PRC2 targets. RNA-seq profiling revealed a significant overlap between DEGs caused by CRISPR–Cas9-induced *EZH2* KO and those by treatment with MS177, but not C24, in EOL-1 cells (Fig. 5k,l, Extended Data Fig. 6e and Supplementary Table 7). Consistently, MS177, but not C24, exhibited de-repression effects on the overall expression of EZH2-repressed transcripts (Fig. 5m,n). Gene set enrichment analysis (GSEA) and GO analyses revealed that MS177 treatment or *EZH2* KO was significantly associated with activation of H3K27me3 or PRC2 targets and with inflammatory or immune response (Fig. 5o,p and Extended Data Fig. 6f–h). EZH2 can regulate immunity[54,55], and quantitative RT–PCR (RT–qPCR) confirmed PRC2 target re-activation after treatment with MS177, but not C24 (Fig. 5q).

Collectively, these results show that MS177 is more effective at inducing EZH2–PRC2 loss and reactivating PRC2–H3K27me3-targeted genes related to antiproliferation and immunity[54,55] compared to inhibitors of the enzymatic function of EZH2.

MS177 also efficiently induces Myc degradation in cancer. MS177-mediated EZH2 degradation occurred at both canonical EZH2–PRC2 sites (Extended Data Fig. 7a) and noncanonical EZH2-solo-binding sites such as *TPD52*, *IRF2BPL* and *GADD45B* (Fig. 6a,b). DEGs downregulated after MS177 treatment were more enriched for genes with EZH2-solo-binding sites than EZH2–PRC2

Fig. 4 | Characterization of the EZH2-targeting PROTAC MS177. a, Structures of C24, MS177, MS177N1 and MS177N2. **b**, EZH2 inhibitory effect of the indicated compound in the in vitro methyltrasferase assay ($n=2$; mean ± s.d.). **c**, Immunoblot of various histone modifications in HeLa cells after a 24-h treatment with the indicated compound (5 μM). **d**, Immunoblot of PRC2 subunits and H3K27 methylation in EOL-1 cells treated with the indicated concentration of MS177, versus DMSO, for 16 h. **e**, Measurement of DC_{50} values of MS177, based on EZH2 immunoblot signals, in EOL-1 cells after treatment ($n=2$; mean ± s.d.). **f**, Immunoblot of EZH2 and H3K27me3 in MV4;11 cells after the indicated compound treatment for 24 h. **g**, Time-dependent EZH2 depletion by MS177 (5 μM) in EOL-1 cells. **h**, EZH2 immunoblot in EOL-1 cells first treated with 0.5 μM of MS177 for 16 h, followed by MS177 washout for the indicated time. **i**, Co-IP for EZH2 interaction with endogenous PRC2 and cMyc in MOLM-13 cells treated with 2.5 μM of DMSO, C24 or MS177N1 for 24 h. IgG (lane 1) serves as IP control. **j**, Top: Ubiquitin (UB) immunoblotting (IB) after IP with anti-EZH2 antibodies using EOL-1 cells after treatment with the indicated compound for 16 h. Bottom: IB using input. **k**,**l**, Immunoblots of PRC2 subunits in MV4;11 (**k**) and EOL-1 (**l**) cells pretreated with DMSO (lanes 1 and 2) or C24 (0.5 μM; lane 3) for 2 h, and then subjected to an additional treatment with DMSO or 2.5 μM of MS177 for 24 (**k**) or 14 h (**l**). **m**,**n**, EZH2 immunoblots using EOL-1 cells pretreated with DMSO (lanes 1 and 3), pomalidomide (2.5 μM, **m**; lanes 2 and 4) or MLN4924 (0.4 μM, **n**; lanes 2 and 4) for 2 h, and then subjected to an additional 14-h treatment with DMSO (lanes 1 and 2) or MS177 (0.5 μM, lanes 3 and 4). **o**, Left: EZH2 immunoblot using MM1.S cells, either WT (left) or with *CRBN* KO (*CRBN*$^{-/-}$; right), after a 24-h treatment with the indicated concentration of MS177. Right: Immunoblot showing *CRBN* KO. Numerical source data and unprocessed blots are available as source data.

targets (Extended Data Fig. 7b). Thus, we reasoned that MS177 may also degrade cMyc, the noncanonical partner of EZH2 at EZH2-solo sites. Indeed, treatment with MS177, but not C24, MS177N1 or MS177N2, significantly decreased cellular cMyc levels (Fig. 6c,d and Extended Data Fig. 7c,d). In agreement with the PRC2-independent binding of EZH2 to cMyc, the EED degrader UNC6852 did not affect the cMyc level but efficiently degraded EED and the associated PRC2 (Fig. 6e). MS177-induced cMyc depletion was significantly suppressed after depletion of CRBN (Fig. 6f) or EZH2 (Fig. 6g). The E3 ligases FBW7, UBR5, SKP2 and HUWE1 can mediate cMyc degradation. However, depletion of these E3 ligases did not interfere with the MS177-mediated cMyc degradation (Extended Data Fig. 7e–g). After washout of MS177, cMyc depletion was recovered (Fig. 6h). Also, cMyc protein was ubiquitinated and then depleted after treatment with MS177, whereas its transcript level was unaltered (Fig. 6i–k). This result supports the idea of a proteasome-mediated degradation mechanism for this effect. The cMyc protein is labile[56,57], and in untreated cells, half-lives of cMyc and EZH2 proteins were measured as ~26 min and ~3.4 h respectively. These half-life values decreased similarly by ~2.2–2.4-fold after MS177 treatment (Fig. 6l,m). Given the striking effect of MS177 on cMyc degradation, we further tested whether MS177 degrades N-Myc, a cMyc-related

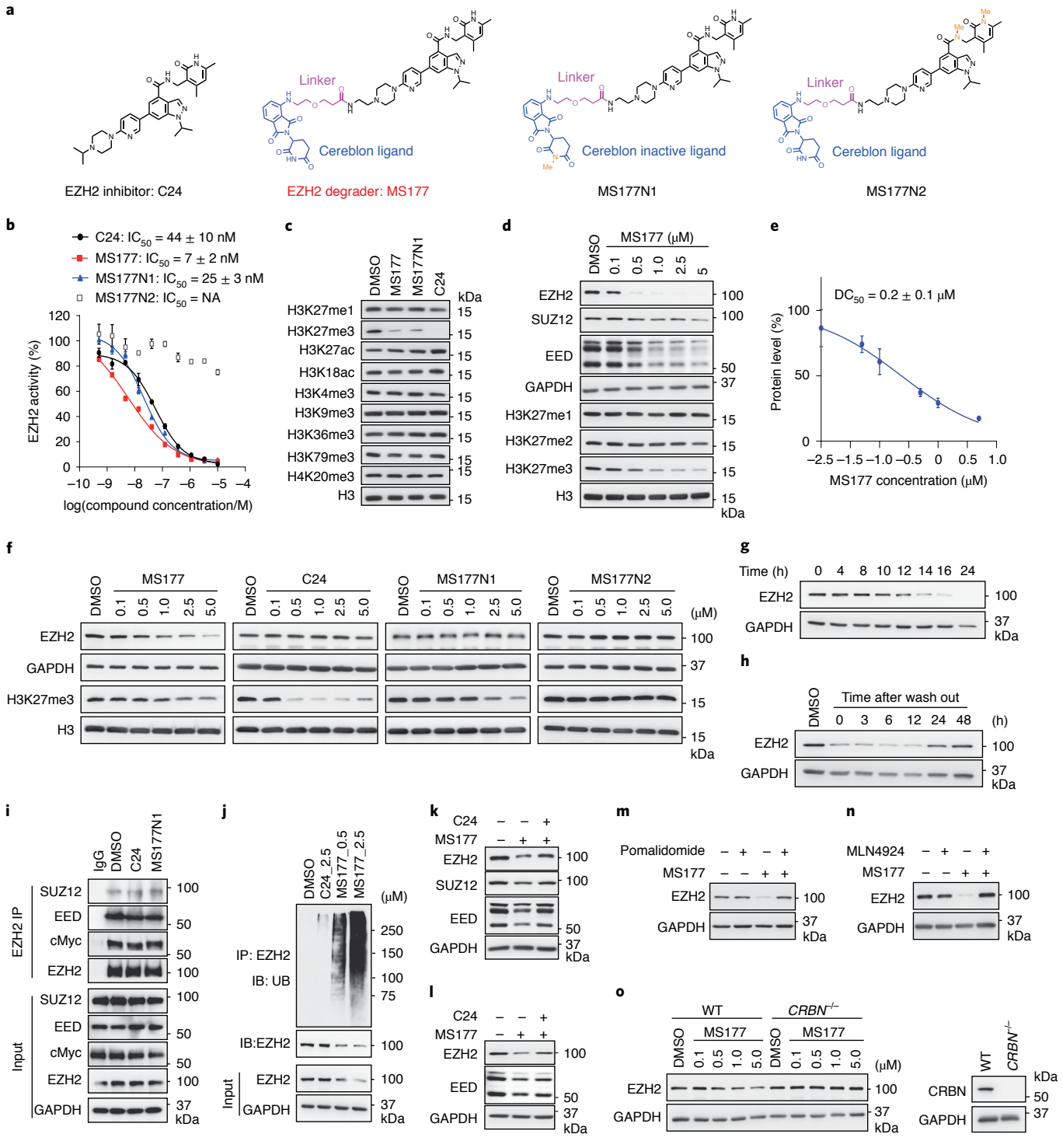

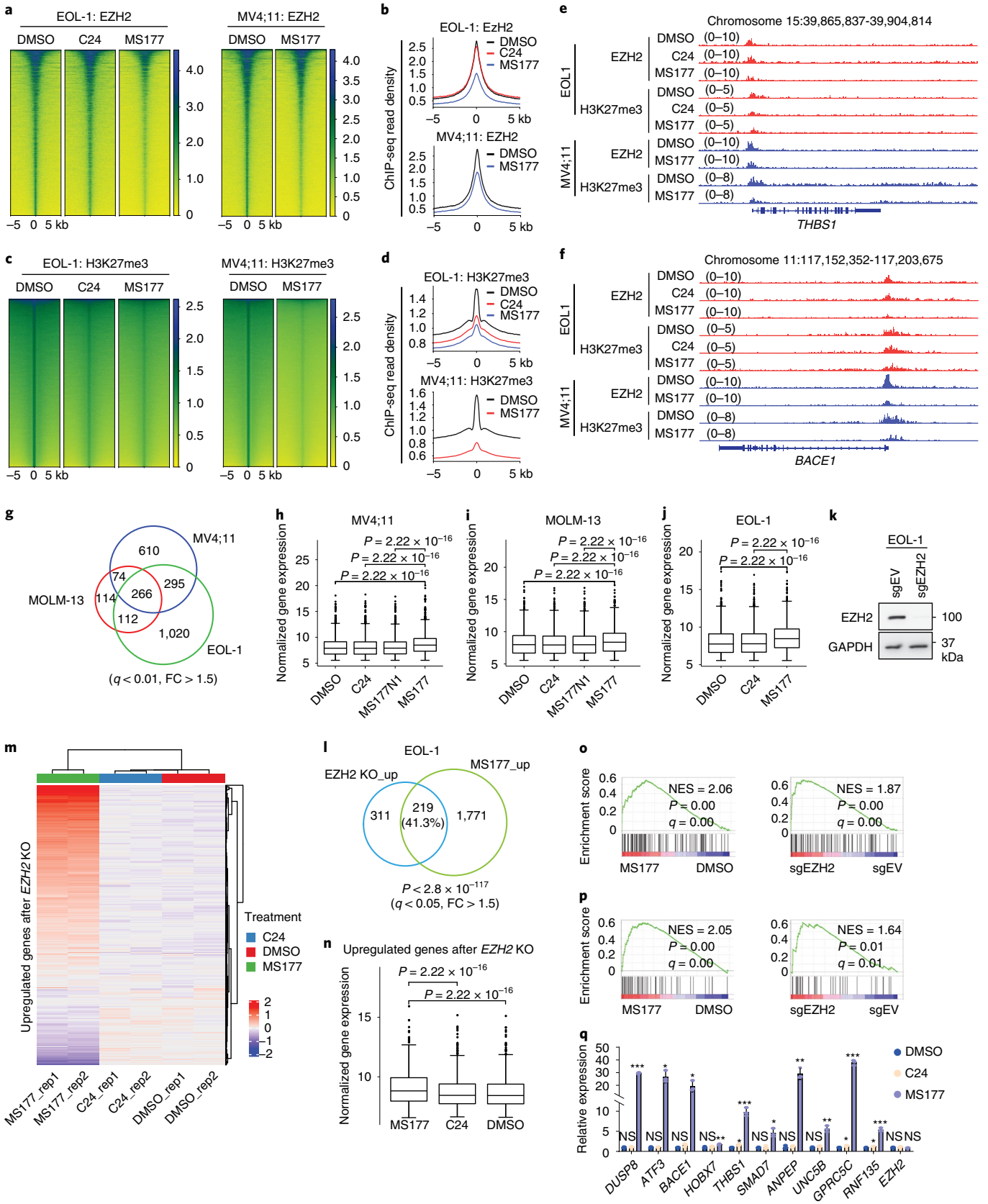

oncogenic TF, by using Kelly cells, a neuroblastoma line in which N-Myc is amplified. Indeed, MS177, but not C24, MS177N1 or MS177N2, degraded both EZH2–PRC2 and N-Myc via ubiquitination in a concentration-dependent manner, which in turn inhibited colony formation of Kelly cells (Extended Data Fig. 7h–k). Notably, cMyc-activated gene-expression programmes were among the most downregulated ones after treatment with MS177 relative to mock treatment in independent MLL-r leukaemia cells, whereas C24

Fig. 5 | MS177 exhibits on-target inhibition of EZH2–PRC2. a–d Heatmaps (**a**,**c**) and averaged plots (**b**,**d**) of EZH2 (**a**,**b**) and H3K27me3 (**c**,**d**) ChIP-seq signal intensities (normalized against spike-in control and sequencing depth) around peak centres in EOL-1 and MV4;11 cells, treated for 16 and 24 h, respectively, with 0.5 μM of DMSO, C24 or MS177. **e**,**f**, IGV views of EZH2 and H3K27me3 at *THBS1* (**e**) and *BACE1* (**f**) in the indicated cells. **g**, Venn diagram using DEGs de-repressed after MS177 versus DMSO treatment, as identified by RNA-seq in the three MLL-r leukaemia lines. Threshold of DEG is set as $q < 0.01$, FC > 1.5 and mean tag counts >10. **h–j**, Overall expression of transcripts upregulated after MS177 versus DMSO treatment across the indicated samples of MV4;11 (**h**), MOLM-13 (**i**) and EOL-1 (**j**) cells. The *y* axis represents $\log_{10}$-converted RNA-seq signals. Paired two-sided *t*-test was used. **k**, Immunoblot showing *EZH2* KO. **l**, Venn diagram using DEGs upregulated (up) in EOL-1 cells after treatment of MS177 and those after *EZH2* KO relative to mock. DEG is defined as above. **m**,**n**, Heatmap (**m**) and boxplot (**n**) showing expression of the EZH2-repressed transcripts in EOL-1 cells, treated with 0.5 μM of DMSO, C24 or MS177 for 16 h ($n = 2$). EZH2-repressed genes are defined in **l** after *EZH2* KO versus mock. Paired two-sided *t*-test was used. Rep, replicate. **o**,**p**, GSEA revealing that MS177 treatment (left) and *EZH2* KO (right) in EOL-1 cells positively correlated with upregulation of the PRC2–EED-repressed (**o**) or H3K27me3-bound (**p**) genes. NES, normalized enrichment score. **q**, RT–qPCR of the EZH2-repressed targets in EOL-1 cells after treatment with 0.5 μM of DMSO, C24 or MS177 for 16 h. The *y* axis shows signals after normalization to GAPDH and to DMSO-treated ($n = 3$; mean ± s.d.; unpaired two-tailed Student's *t*-test). For **h–j** and **n**, the boundaries of boxplots indicate the 25th and 75th percentiles, the centre line indicates the median, and the whiskers (dashed) indicate 1.5× the interquartile range. $^*P < 0.05$, $^{**}P < 0.01$ and $^{***}P < 0.005$. Numerical source data, statistics, exact *P* values and unprocessed blots are available as source data.

did not have such effect (Fig. 6n and Extended Data Fig. 7l,m). RT–qPCR verified the downregulation effect by MS177, but not C24 or MS177N1, on the cMyc-activated targets (Fig. 6o).

Overall, compared to inhibitors of the enzymatic function of EZH2, MS177 induces Myc ubiquitination and degradation, which in turn suppresses the Myc-enforced oncogenic circuitry.

MS177 is more effective than EZH2 inhibitors in killing tumour cells. Next, we evaluated the cancer-killing capacity of MS177. In a panel of MLL-r leukaemia cell lines and samples from patients with AML (Supplementary Table 8), MS177 displayed potent, fast-acting and consistent antiproliferation effects, whereas C24 and MS177N1 generally had no effect on EZH2 or cMyc degradation and had little to mild effects in tumour cell killing (Fig. 6d and Extended Data Figs. 4a–c and 8a). Strikingly, half-maximal effective concentration (EC_{50}) values of MS177 showed two-to-three orders of magnitude increase in potency compared with those for C24, MS177N1 and MS177N2 (Supplementary Table 9, Fig. 7a–c and Extended Data Fig. 8b,c). Additionally, a much weaker effect of MS177 was seen with samples from patients in remission (which were mainly healthy cells) compared with paired AML samples (Fig. 7d,e). Degradation of PRC2 and cMyc, as well as de-repression of EZH2–PRC2 target genes, was observed in patient samples after treatment with MS177, but not C24, relative to treatment with dimethyl sulfoxide (DMSO) (Fig. 7f,g and Extended Data Fig. 8d,e). Furthermore, MS177 was more potent in inhibiting leukaemia growth than a panel of EZH2 catalytic inhibitors and an EED degrader, although all of them effectively abolished H3K27me3 (Fig. 7h–j). Notably, MS177 had little inhibitory effect on colony formation in primary haematopoietic stem and progenitor cells (HSPCs) or on the growth of K562 cells (Fig. 7k and Extended Data Fig. 8f,g), which suggests that MS177 lacks general cytotoxicity. IKZF1 and IKZF3 are known neo-substrates of CRBN[58], the E3 ligase that MS177 recruits. Although MS177, MS177N2 and pomalidomide all induced IKZF1 and IKZF3 degradation, only MS177 markedly inhibited the growth of MLL-r leukaemia cells (Fig. 7l,m and Extended Data Fig. 8h,i), which suggests that the MS177-induced tumour-killing effect does not stem from the degradation of the neo-substrates of CRBN. Furthermore, only MS177 treatment (that is, not C24 or MS177N1) decreased colony-forming capabilities, slowed cell cycle progression and induced leukaemia cell apoptosis (Fig. 7n–q and Extended Data Fig. 8j–l). Meanwhile, EZH2 depletion greatly diminished the MS177-mediated apoptotic and antiproliferation effects (Fig. 7r and Extended Data Fig. 8m), which again provides support for concept that the antitumour effect of MS177 depends on EZH2 binding. Together, these results show that the cancer-killing effects of MS177 are more potent and fast-acting than inhibitors of the enzymatic function of EZH2.

MS177 represses tumour growth in vivo. Next, we characterized the pharmacokinetic properties of MS177 in mice. Intraperitoneal (i.p.) injection of MS177 at a dose of 50 mg per kg achieved intraplasma concentrations comparable to the EC_{50} value measured in vitro in cancer cells (Fig. 8a and Supplementary Table 10). Furthermore, two doses of MS177 (100 mg per kg i.p. twice a day (BID) for 6 days per week; and 200 mg per kg i.p. BID 3 days per week) were well tolerated and lacked apparent toxicity in mice (Extended Data Fig. 9a,b). Next, we assessed the antitumour effect of MS177 using a PDX animal model of MLL-r AML (Extended Data Fig. 9c,d). Relative to vehicle treatment, the above two regimens of MS177 dosing significantly inhibited AML growth in PDX models, which were established via dissemination or subcutaneously, and prolonged survival

Fig. 6 | MS177 represses the cMyc-related oncogenic node. a, Heatmaps showing EZH2 ChIP-seq signals around the centres of EZH2-solo-binding peaks in EOL-1 (left) and MV4;11 (right) cells, treated for 16 and 24 h, respectively, with 0.5 μM of DMSO, C24 or MS177. **b**, EZH2 binding at *TPD52*, *IRF2BPL* and *GADD45B* in the indicated cells. **c**,**d**, cMyc immunoblots of MV4;11 (**c**) and EOL-1 (**d**) cells after treatment with the indicated compound. **e**, Immunoblots of the indicated protein in EOL-1 cells treated with an EED-targeting PROTAC (UNC6852) or its non-PROTAC analogue (UNC7043) for 24 h. **f**, cMyc immunoblots of WT or CRBN-deficient ($CRBN^{-/-}$) MM1.S cells treated with MS177 versus DMSO for 24 h. **g**, Left: Immunoblot showing *EZH2* KO. Right: cMyc immunoblot using EZH2-depleted or mock-treated MOLM-13 cells treated with 5 μM of MS177 for 6 or 8 h versus DMSO. **h**, cMyc immunoblot of EOL-1 cells first treated with 0.5 μM of MS177 for 16 h and then subjected to MS177 washout for the indicated time compared to DMSO-treated mock. **i**, cMyc ubiquitination immunoblot of EOL-1 cells treated with 5 μM of MS177 versus DMSO for 4 h. **j**,**k**, Immunoblot (**j**) and RT–PCR for cMyc (**k**; $n = 3$; mean ± s.d.) in EOL-1 and MV4;11 cells treated with 5 μM of MS177 versus DMSO for 4 h. **l**,**m**, Immunoblots (left) and degradation curve (right) of cMyc (**l**) or EZH2 (**m**) in DMSO- or MS177 (5 μM)-treated EOL-1 cells in the presence of cycloheximide (CHX; $n = 2$ independent experiments; mean ± s.d.). **n**, Summary of GSEA results showing the correlation of the indicated Myc-related gene sets with MS177 treatment or *cMyc* KO (sgcMyc) relative to mock. Green and red in the heatmap indicate positive and negative correlations, respectively. **o**, RT–qPCR of cMyc-mediated upregulated targets in MV4;11 cells after treatment with the indicated compound for 24 h. The *y* axis shows signals after normalization to GAPDH and to DMSO-treated cells ($n = 3$; mean ± s.d.; unpaired two-tailed Student's *t*-test). $^*P < 0.05$, $^{**}P < 0.01$ and $^{***}P < 0.005$. Numerical source data, statistics, exact *P* values and unprocessed blots are available as source data.

(Fig. 8b–f and Extended Data Fig. 9e,f). Similar tumour-suppressing effects by MS177 were observed in additional subcutaneously xenografted MLL-r leukaemia models using RS4;11 or EOL-1 cells (Fig. 8g,h and Extended Data Fig. 9g). During dosing, the intratumour and intraplasma MS177 concentrations were measured as ~3–5 μM, and we observed the expected effect of MS177 on the degradation of EZH2–PRC2 and cMyc and on the modulation of EZH2 target genes in the tumour xenografts (Fig. 8i–k and Extended Data Fig. 9h). Together, the EZH2-targeting PROTAC MS177 is an effective therapeutic agent that does not show significant general toxicity.

Discussion

Extensive evidence points to the tumour-promoting roles of EZH2 in human cancer. Patients with higher EZH2 expression often display poorer clinical outcomes[3–6,59]. Canonically, EZH2 serves as the enzymatic subunit of PRC2 for catalysing H3K27me3 and repressing gene expression. Increasing evidence shows that EZH2 also relies on methyltransferase-independent mechanisms to modulate gene expression and oncogenesis[10,20,23–27], as exemplified by its gene-activating roles at NF-κB[23] and androgen receptor[10] targets in solid cancers. Here, we unveiled that in MLL-r leukaemias, EZH2 uses a hidden TAD to

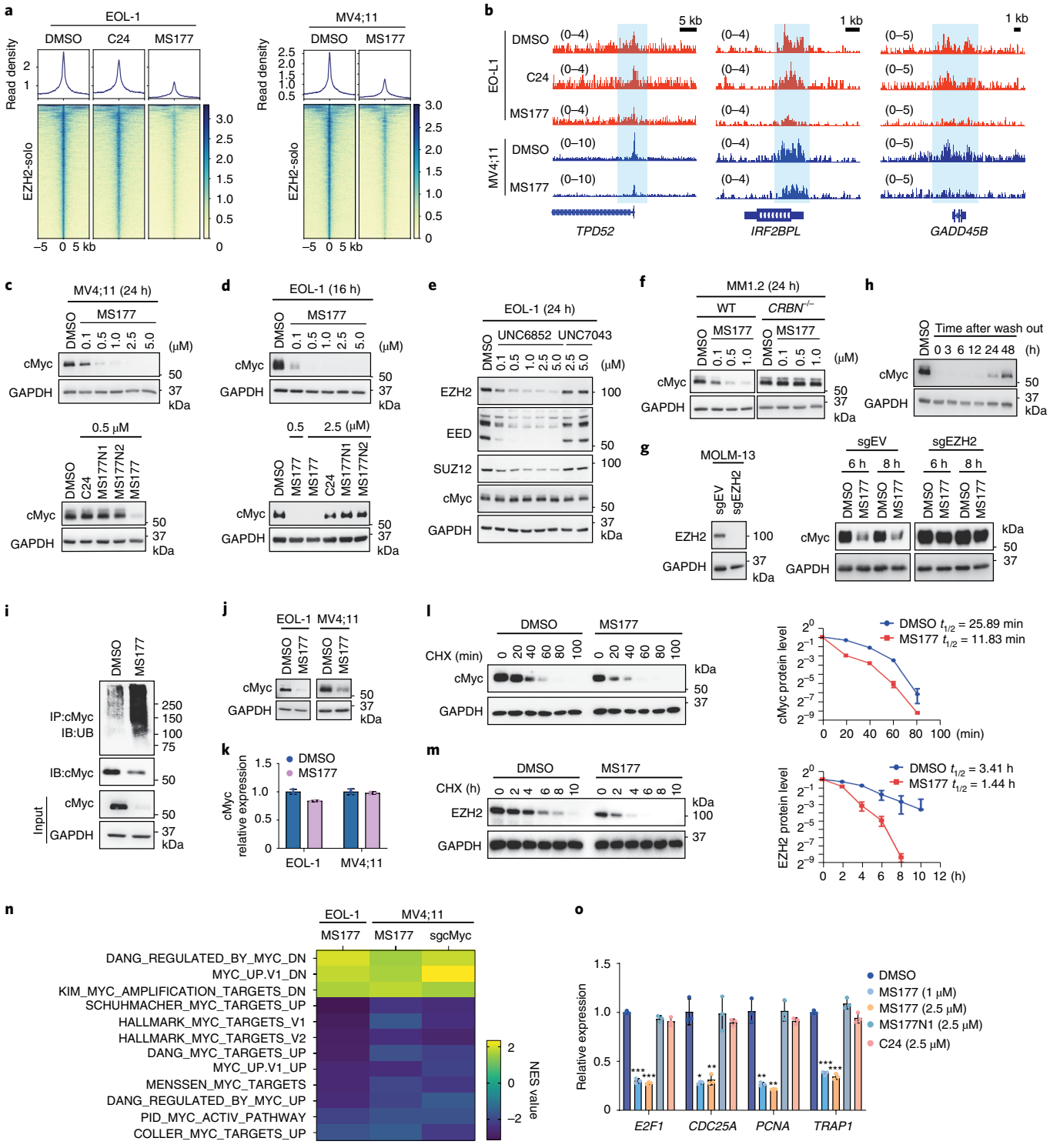

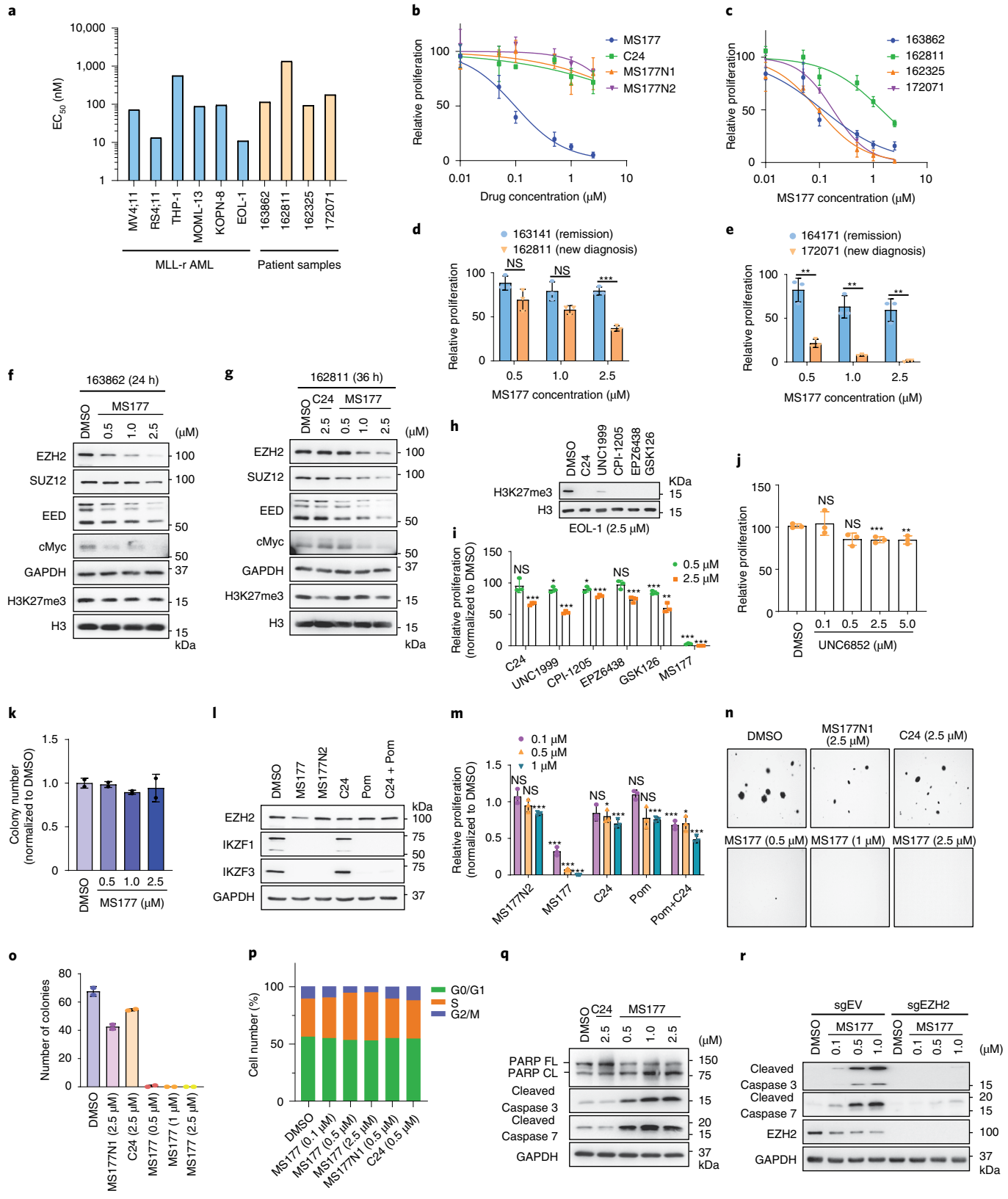

interact with cMyc and p300 and to activate AML-related transcripts. To our knowledge, a direct EZH2–cMyc interaction and the involvement of EZH2-TAD to regulate its noncanonical targets and promote oncogenesis have not been reported. We speculate that such unconventional functions of EZH2 might be due to EZH2 overexpression in aggressive cancers and a lack of concurrently increased levels of other PRC2 subunits. This in turn shifts the PRC2 component stoichiometry, which may be further enhanced by the cMyc upregulation that exists in cancer. Cellular contexts such as kinase signalling also regulate the EZH2 interaction with PRC2 subunits[20].

Fig. 7 | MS177 efficiently induces leukaemia cell growth inhibition, apoptosis and cell cycle progression arrest. a, EC_{50} values of MS177 in the indicated AML cell lines (left) and patient samples (right) after 4 days of treatment ($n=3$). **b**, MOLM-13 cell growth after a 48-h treatment with different concentrations of C24, MS177, MS177N1 or MS177N2 relative to DMSO. The *y* axis shows mean ± s.d. after normalization to DMSO-treated cells ($n=3$). **c**–**e**, Effect of a 48-h treatment with various concentration of MS177, relative to DMSO, on the proliferation of four primary AML samples (**c**) or paired cells from de-identified patients, either in remission or diagnosed with AML (**d**,**e**).The *y* axis shows mean ± s.d. after normalization to mock ($n=3$). **f**,**g**, Immunoblots of the indicated protein in two primary AML samples treated with DMSO, MS177 or C24 for 24 h (**f**) or 36 h (**g**). **h**–**j**, H3K27me3 immunoblot (**h**) and growth (**i**,**j**) of EOL-1 cells treated with the indicated concentration of various EZH2 catalytic inhibitors (**h**,**i**), MS177 (**i**) or UNC6852 (**j**) for 48 h ($n=3$; mean ± s.d.; unpaired two-tailed Student's *t*-test). **k**, Colony formation by murine HSPCs in the presence of DMSO or MS177 ($n=2$; mean ± s.d.). **l**,**m**, Immunoblot of the indicated protein (**l**) and growth (**m**) of MV4;11 cells treated with 2.5 μM of DMSO, MS177, MS177N2, C24, pomalidomide (Pom) or C24 plus Pom for 48 h. The *y* axis in **k** shows mean ± s.d. after normalization to DMSO-treated cells ($n=3$; unpaired two-tailed Student's *t*-test). **n**,**o**, Representative image (**n**) and quantification of colony formation (**o**; mean ± s.d. of two experiments) using MV4;11 cells treated with the indicated compound. **p**, MOLM-13 cell cycle analysis after a 24-h treatment with the indicated compounds. **q**,**r**, Immunoblots of various apoptotic markers after treatment of cells from a patient with AML (162325; **q**), or of MOLM-13 cells with the mock-treated (sgEV) or EZH2-depleted (sgEZH2) (**r**), with the indicated compound for 24 h. $^{*}P<0.05$, $^{**}P<0.01$ and $^{***}P<0.005$. Numerical source data, statistics, exact *P* values and unprocessed blots are available as source data.

A thorough understanding of the multifaceted actions of EZH2 is important for developing more effective therapies for the treatment of EZH2-dependent cancers. Small-molecule inhibitors of EZH2 effectively inhibit its methyltransferase activity but cannot suppress its methyltransferase-independent functions. Consequently, inhibitors of the catalytic function of EZH2 show slow and often incomplete tumour-suppressive effects. We used the PROTAC technology and discovered a highly effective EZH2-targeting degrader, MS177, in addition to two structurally similar analogues, MS177N1 (which binds EZH2 but not CRBN) and MS177N2 (which binds CRBN but not EZH2), as controls. We comprehensively characterized their effects in vitro and in vivo. First, MS177 potently degrades EZH2 and EZH2-associated partners (PRC2 and cMyc), and MS177 is highly selective for EZH2 compared to approximately 100 proteins that covered methyltransferases and common drug targets. Second, in a range of cancer lines and patient-derived models, MS177 demonstrated stronger antitumour effects compared with catalytic inhibitors of EZH2 and non-degrader analogues of MS177. Third, integrated genomic profiling showed that MS177 effectively depletes chromatin-bound EZH2 and displays a more substantial effect on re-activating EZH2–PRC2 targets compared with inhibitors of the enzymatic function of EZH2. Fourth, MS177 not only displayed notable pharmacokinetic and pharmacodynamic relationships and is well tolerated in vivo but it also suppressed the in vivo oncogenesis of multiple tumour cell line xenografted and PDX models and enhanced overall survival. MS177 therefore represents a promising therapeutic agent for further development. Fifth, compared with catalytic inhibitors of EZH2 and an EED-targeting PROTAC, MS177 suppressed Myc-related oncogenic programmes in cancer. The Myc-suppressing effect is due to a direct interaction with the EZH2-TAD and cMyc. As the EZH2-TAD–cMyc interaction is PRC2-independent and related to transactivation, this noncanonical function of EZH2 is generally unaffected by catalytic inhibitors of EZH2 or the EED degrader. Together, our findings highlight the advantages of the EZH2-targeting PROTAC over its catalytic inhibitors as a therapeutic. An effective EZH2 PROTAC degrader simultaneously targets the multifaceted oncogenic functions of EZH2, which leads to more effective, consistent and fast-acting antitumour effects compared with catalytic inhibitors of EZH2 (see the schematic in Fig. 8l).

The mechanisms underlying the recruitment of cMyc to EZH2-solo-binding sites are complex. Although canonical cMyc motifs were enriched at EZH2-solo-binding peaks, studies have demonstrated that cMyc-binding sites in cells often lack such motifs. We uncovered a direct interaction of EZH2-TAD with cMyc-CD. cMyc can interact, either directly or indirectly, with the basal transcription machinery, with activators and cofactors and with transcriptional elongation factors[36,41–43]. In agreement, EZH2-TAD directly bound (co)activators such as p300 and cMyc. Conceivably, these biochemical interactions collectively contribute to the co-targeting of cMyc and EZH2 to EZH2-solo-binding sites where (co)activators, Pol II and gene-activation-related markers coexist. A 'coalition model' has been proposed, whereby multiple cooperating interactions exist among cMyc and many partners during oncogenesis[36]. TADs of (co)activators are often unstructured, and intrinsically disorganized protein regions can induce phase separation as has been proposed for cMyc[36,39]. We speculate that the TAD and/or the unstructured protein region of EZH2, cMyc and (co)activators establish phase-separated condensates to mediate gene activation. It is also worth highlighting the multifaceted nature of the biological functions of cMyc besides its most-studied role in transcriptional regulation[36,39]. In agreement, our RNA-seq results suggested that cMyc does not always display a potent transcriptional activation role at cMyc–EZH2-solo cobound genes, which merits further investigation. Here, an exciting finding is that

Fig. 8 | MS177 represses AML growth in vivo. a, Intraplasma concentrations of MS177 over a 12-h period after a single indicated i.p. injection (50 mg per kg) into male Swiss Albino mice ($n=6$; mean ± s.e.m. from 3 mice per time point). **b**–**d**, Bioluminescent images (**b**) and signal levels (**c**) and Kaplan–Meier curves (**d**) of NSG-SGM3 mice transplanted intravenously (i.v.) with the luciferase-labelled MLL-r AML PDX cells (PDX 68555-luc), which were then treated with vehicle or the indicated MS177 dosage ($n=5$ mice per group; mean ± s.d.). Statistical significance was determined by two-way analysis of variance (ANOVA; **c**) or log-rank (Mantel–Cox, **d**) test. **e**–**h**, Averaged tumour volume (**e**,**g**,**h**) and Kaplan–Meier curve (**f**) of mice subcutaneously (s.c.) transplanted with PDX 68555 cells (**e**,**f**), RS4;11 (**g**) or EOL-1 cells (**h**), which were then treated with vehicle or the indicated MS177 dosage ($n=5$ per group; mean ± s.d.). Statistical significance was determined by two-way ANOVA (**e**), log-rank test (**f**) or unpaired two tailed Student's *t*-test (**h;** boxplot shows mean and interquartile range). **i**, Immunoblots of the indicated protein using the collected RS4;11 s.c. xenografted tumours, freshly isolated from NSG mice that were treated with vehicle or the indicated MS177 dosage for 5 days. **j**, Intraplasma and intratumour concentrations of MS177 in NSG mice in **h**, treated with vehicle or the indicated MS177 dosing ($n=4$ per group). Dots represent individual tumours. **k**, RT–qPCR for the EZH2-repressed target in the EOL-1 s.c. xenografted tumours isolated in **i**. The *y* axis shows the mean ± s.d. after normalization to GAPDH and then to vehicle-treated samples ($n=3$; unpaired two-tailed Student's *t*-test). **l**, A model showing that in MLL-r leukaemias, EZH2 forms canonical (EZH2–PRC2) and noncanonical (EZH2–cMyc–coactivators) interactions to promote target gene repression and activation, respectively, both of which mediate oncogenesis (top). These oncogenic actions of EZH2 can be suppressed by the EZH2 PROTAC degrader MS177 (bottom). $^{*}P<0.05$, $^{**}P<0.01$ and $^{***}P<0.005$. Numerical source data, statistics, exact *P* values and unprocessed blots are available as source data.

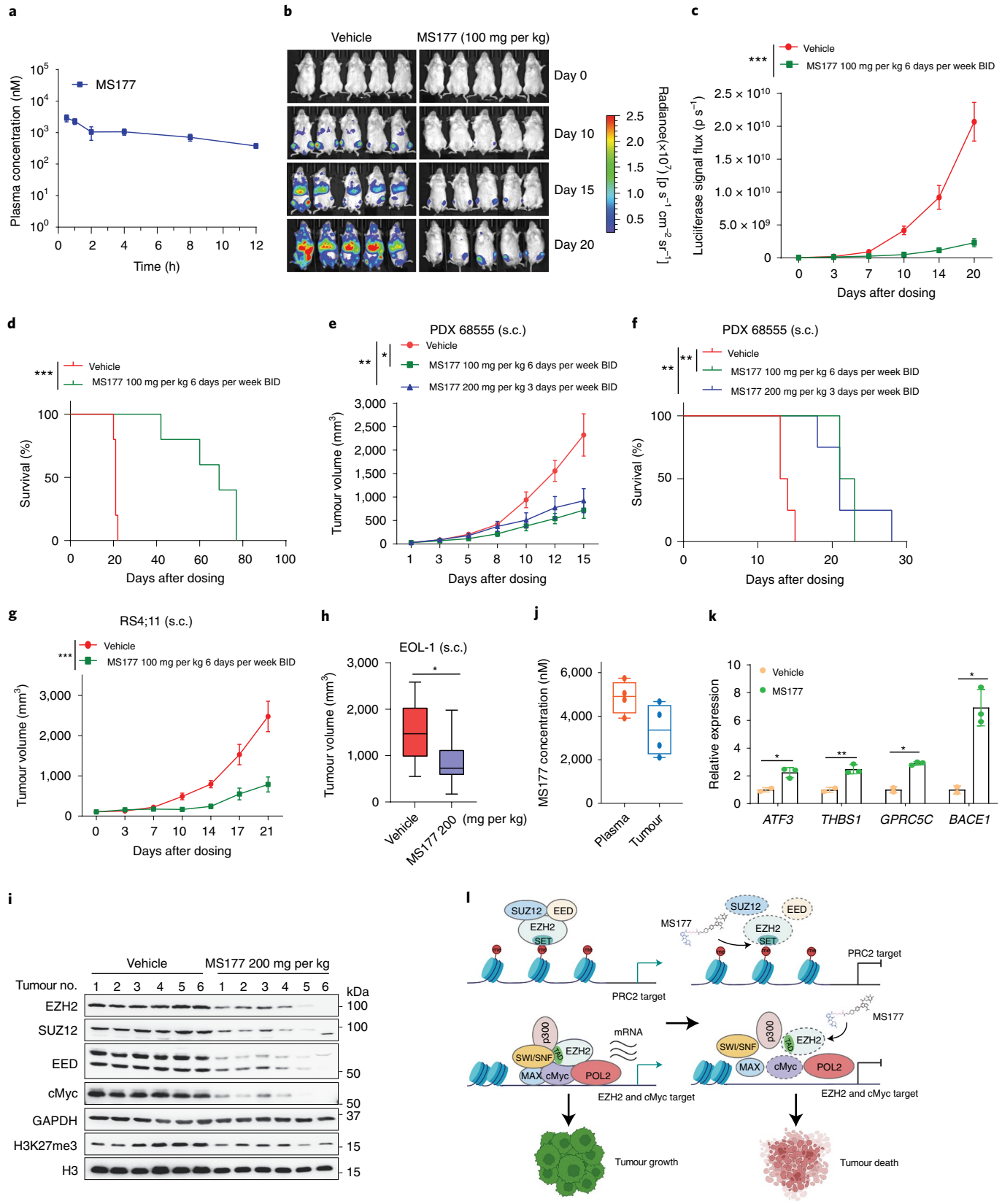

an EZH2-targeting PROTAC effectively degrades Myc, which adds to the limited arsenal of compounds that target Myc[36].

We carefully assessed the MOA of MS177. Depletion of cellular CRBN or EZH2, to which MS177 binds, abolished the effects of MS177 on EZH2 and cMyc degradation, as well as apoptosis induction and antiproliferation. This result provides support for a CRBN-dependent and EZH2-binding-dependent MOA. MS177 degrades EZH2 at both canonical EZH2–PRC2 and noncanonical EZH2-solo-binding sites, with the effect being more striking at the latter. Also, the cMyc-degrading effect of MS177 appears to be more

apparent. Such differential degradation effects by MS177 could potentially be caused by several factors. First, PROTAC access to targets (the SET domain of EZH2 to MS177) is context-dependent. Conceivably, EZH2–PRC2-bound chromatin is in a more closed conformation compared with EZH2-solo-bound regions, which may affect compound access. Second, protein or complex stability varies drastically. cMyc protein, with a half-life of ~30 min in cells, is more labile than EZH2, which may partly explain why cMyc appears to be degraded faster after MS177 treatment. In fact, MS177 had the same effects on decreasing the half-lives of EZH2 and cMyc proteins. Notably, cMyc proteins are highly mobile in cells[60], and it may be that the cellular pool of cMyc can be efficiently 'drained' through MS177-mediated degradation of EZH2–cMyc. Overall, MS177, which effectively degrades both EZH2 and cMyc, is a promising therapeutic agent for treating EZH2-dependent cancers.

Online content

Any methods, additional references, Nature Research reporting summaries, source data, extended data, supplementary information, acknowledgements, peer review information; details of author contributions and competing interests; and statements of data and code availability are available at https://doi.org/10.1038/s41556-022-00850-x.

Received: 29 July 2021; Accepted: 14 January 2022;
Published online: 24 February 2022

References

1. Yu, J. R., Lee, C. H., Oksuz, O., Stafford, J. M. & Reinberg, D. PRC2 is high maintenance. *Genes Dev.* **33**, 903–935 (2019).
2. Guo, Y., Zhao, S. & Wang, G. G. Polycomb gene silencing mechanisms: PRC2 chromatin targeting, H3K27me3 'readout', and phase separation-based compaction. *Trends Genet.* **37**, 547–565 (2021).
3. Kim, K. H. & Roberts, C. W. Targeting EZH2 in cancer. *Nat. Med.* **22**, 128–134 (2016).
4. Xu, B., Konze, K. D., Jin, J. & Wang, G. G. Targeting EZH2 and PRC2 dependence as novel anticancer therapy. *Exp. Hematol.* **43**, 698–712 (2015).
5. Wang, X. et al. Clinical and prognostic relevance of EZH2 in breast cancer: a meta-analysis. *Biomed. Pharmacother.* **75**, 218–225 (2015).
6. Varambally, S. et al. The Polycomb group protein EZH2 is involved in progression of prostate cancer. *Nature* **419**, 624–629 (2002).
7. Beguelin, W. et al. EZH2 is required for germinal center formation and somatic *EZH2* mutations promote lymphoid transformation. *Cancer Cell* **23**, 677–692 (2013).
8. Neff, T. et al. Polycomb repressive complex 2 is required for MLL-AF9 leukemia. *Proc. Natl Acad. Sci. USA* **109**, 5028–5033 (2012).
9. Shi, J. et al. The Polycomb complex PRC2 supports aberrant self-renewal in a mouse model of MLL-AF9;Nras^{G12D} acute myeloid leukemia. *Oncogene* **32**, 930–938 (2013).
10. Xu, K. et al. EZH2 oncogenic activity in castration-resistant prostate cancer cells is Polycomb-independent. *Science* **338**, 1465–1469 (2012).
11. Bhat, K. P., Umit Kaniskan, H., Jin, J. & Gozani, O. Epigenetics and beyond: targeting writers of protein lysine methylation to treat disease. *Nat. Rev. Drug Discov.* **20**, 265–286 (2021).
12. Knutson, S. K. et al. A selective inhibitor of EZH2 blocks H3K27 methylation and kills mutant lymphoma cells. *Nat. Chem. Biol.* **8**, 890–896 (2012).
13. Knutson, S. K. et al. Durable tumor regression in genetically altered malignant rhabdoid tumors by inhibition of methyltransferase EZH2. *Proc. Natl Acad. Sci. USA* **110**, 7922–7927 (2013).
14. McCabe, M. T. et al. EZH2 inhibition as a therapeutic strategy for lymphoma with EZH2-activating mutations. *Nature* **492**, 108–112 (2012).
15. Konze, K. D. et al. An orally bioavailable chemical probe of the lysine methyltransferases EZH2 and EZH1. *ACS Chem. Biol.* **8**, 1324–1334 (2013).
16. Yang, X. et al. Structure–activity relationship studies for enhancer of zeste homologue 2 (EZH2) and enhancer of zeste homologue 1 (EZH1) inhibitors. *J. Med. Chem.* **59**, 7617–7633 (2016).
17. Vaswani, R. G. et al. Identification of (*R*)-*N*-((4-methoxy-6-methyl-2-oxo-1,2-dihydropyridin-3-yl)methyl)−2-methyl-1-(1-(1 -(2,2,2-trifluoroethyl) piperidin-4-yl)ethyl)-1*H*-indole-3-carboxamide (CPI-1205), a potent and selective inhibitor of histone methyltransferase EZH2, suitable for Phase I clinical trials for B-cell lymphomas. *J. Med. Chem.* **59**, 9928–9941 (2016).
18. Xu, B. et al. Selective inhibition of EZH2 and EZH1 enzymatic activity by a small molecule suppresses MLL-rearranged leukemia. *Blood* **125**, 346–357 (2015).
19. Garapaty-Rao, S. et al. Identification of EZH2 and EZH1 small molecule inhibitors with selective impact on diffuse large B cell lymphoma cell growth. *Chem. Biol.* **20**, 1329–1339 (2013).
20. Wang, J. & Wang, G. G. No easy way out for EZH2: its pleiotropic, noncanonical effects on gene regulation and cellular function. *Int. J. Mol. Sci.* **21**, 9501 (2020).
21. Lee, S. T. et al. Context-specific regulation of NF-κB target gene expression by EZH2 in breast cancers. *Mol. Cell* **43**, 798–810 (2011).
22. Gonzalez, M. E. et al. EZH2 expands breast stem cells through activation of NOTCH1 signaling. *Proc. Natl Acad. Sci. USA* **111**, 3098–3103 (2014).
23. Lawrence, C. L. & Baldwin, A. S. Non-canonical EZH2 transcriptionally activates RelB in triple negative breast cancer. *PLoS ONE* **11**, e0165005 (2016).
24. Yan, J. et al. EZH2 overexpression in natural killer/T-cell lymphoma confers growth advantage independently of histone methyltransferase activity. *Blood* **121**, 4512–4520 (2013).
25. Zhao, Y. et al. EZH2 cooperates with gain-of-function p53 mutants to promote cancer growth and metastasis. *EMBO J.* **38**, e99599 (2019).
26. Kim, J. et al. Polycomb- and methylation-independent roles of EZH2 as a transcription activator. *Cell Rep.* **25**, 2808–2820.e2804 (2018).
27. Kim, K. H. et al. SWI/SNF-mutant cancers depend on catalytic and non-catalytic activity of EZH2. *Nat. Med.* **21**, 1491–1496 (2015).
28. Krivtsov, A. V. & Armstrong, S. A. MLL translocations, histone modifications and leukaemia stem-cell development. *Nat. Rev. Cancer* **7**, 823–833 (2007).
29. Rao, R. C. & Dou, Y. Hijacked in cancer: the KMT2 (MLL) family of methyltransferases. *Nat. Rev. Cancer* **15**, 334–346 (2015).
30. Lai, A. C. & Crews, C. M. Induced protein degradation: an emerging drug discovery paradigm. *Nat. Rev. Drug Discov.* **16**, 101–114 (2017).
31. Schapira, M., Calabrese, M. F., Bullock, A. N. & Crews, C. M. Targeted protein degradation: expanding the toolbox. *Nat. Rev. Drug Discov.* **18**, 949–963 (2019).
32. Chamberlain, P. P. & Hamann, L. G. Development of targeted protein degradation therapeutics. *Nat. Chem. Biol.* **15**, 937–944 (2019).
33. Dale, B. et al. Advancing targeted protein degradation for cancer therapy. *Nat. Rev. Cancer* **21**, 638–654 (2021).
34. Skene, P. J., Henikoff, J. G. & Henikoff, S. Targeted in situ genome-wide profiling with high efficiency for low cell numbers. *Nat. Protoc.* **13**, 1006–1019 (2018).
35. Allevato, M. et al. Sequence-specific DNA binding by MYC/MAX to low-affinity non-E-box motifs. *PLoS ONE* **12**, e0180147 (2017).
36. Lourenco, C. et al. MYC protein interactors in gene transcription and cancer. *Nat. Rev. Cancer* **21**, 579–591 (2021).
37. Pellanda, P. et al. Integrated requirement of non-specific and sequence-specific DNA binding in Myc-driven transcription. *EMBO J.* **40**, e105464 (2021).
38. Sabò, A. & Amai, B. Genome recognition by MYC. *Cold Spring Harb. Perspect. Med.* **4**, a014191 (2014).
39. Baluapuri, A., Wolf, E. & Eilers, M. Target gene-independent functions of MYC oncoproteins. *Nat. Rev. Mol. Cell Biol.* **21**, 255–267 (2020).
40. Guo, J. et al. Sequence specificity incompletely defines the genome-wide occupancy of Myc. *Genome Biol.* **15**, 482 (2014).
41. Rahl, P. B. & Young, R. A. MYC and transcription elongation. *Cold Spring Harb. Perspect. Med* **4**, a020990 (2014).
42. Kalkat, M. et al. MYC protein interactome profiling reveals functionally distinct regions that cooperate to drive tumorigenesis. *Mol. Cell* **72**, 836–848.e7 (2018).
43. Baluapuri, A. et al. MYC recruits SPT5 to RNA polymerase II to promote processive transcription elongation. *Mol. Cell* **74**, 674–687.e11 (2019).
44. Lin, C. Y. et al. Transcriptional amplification in tumor cells with elevated c-Myc. *Cell* **151**, 56–67 (2012).
45. Potjewyd, F. et al. Degradation of Polycomb repressive complex 2 with an EED-targeted bivalent chemical degrader. *Cell Chem. Biol.* **27**, 47–56.e15 (2020).
46. Lasko, L. M. et al. Discovery of a selective catalytic p300/CBP inhibitor that targets lineage-specific tumours. *Nature* **550**, 128–132 (2017).
47. Piskacek, M., Otasevic, T., Repko, M. & Knight, A. The 9aaTAD activation domains in the Yamanaka transcription factors Oct4, Sox2, Myc, and Klf4. *Stem Cell Rev. Rep.* **17**, 1934–1936 (2021).
48. Jiao, L. et al. A partially disordered region connects gene repression and activation functions of EZH2. *Proc. Natl Acad. Sci. USA* **117**, 16992–17002 (2020).
49. Tanaka, S. et al. Ezh2 augments leukemogenicity by reinforcing differentiation blockage in acute myeloid leukemia. *Blood* **120**, 1107–1117 (2012).
50. Ma, A. et al. Discovery of a first-in-class EZH2 selective degrader. *Nat. Chem. Biol.* **16**, 214–222 (2020).
51. Winter, G. E. et al. Drug development. Phthalimide conjugation as a strategy for in vivo target protein degradation. *Science* **348**, 1376–1381 (2015).
52. Fischer, E. S. et al. Structure of the DDB1–CRBN E3 ubiquitin ligase in complex with thalidomide. *Nature* **512**, 49–53 (2014).

53. Soucy, T. A. et al. An inhibitor of NEDD8-activating enzyme as a new approach to treat cancer. *Nature* **458**, 732–736 (2009).
54. Ennishi, D. et al. Molecular and genetic characterization of MHC deficiency identifies EZH2 as therapeutic target for enhancing immune recognition. *Cancer Discov.* **9**, 546–563 (2019).
55. Burr, M. L. et al. An evolutionarily conserved function of Polycomb silences the MHC class I antigen presentation pathway and enables immune evasion in cancer. *Cancer Cell* **36**, 385–401.e8 (2019).
56. Gu, Y. et al. Stabilization of the c-Myc Protein by CAMKIIγ Promotes T Cell Lymphoma. *Cancer Cell* **32**, 115–128.e117 (2017).
57. Jiang, J. et al. Direct phosphorylation and stabilization of MYC by Aurora B kinase promote T-cell leukemogenesis. *Cancer Cell* **37**, 200–215.e5 (2020).
58. Kronke, J. et al. Lenalidomide causes selective degradation of IKZF1 and IKZF3 in multiple myeloma cells. *Science* **343**, 301–305 (2014).
59. Jiang, T. et al. Prognostic value of high EZH2 expression in patients with different types of cancer: a systematic review with meta-analysis. *Oncotarget* **7**, 4584–4597 (2016).
60. Izeddin, I. et al. Single-molecule tracking in live cells reveals distinct target-search strategies of transcription factors in the nucleus. *eLife* **3**, e02230 (2014).

Methods

All animal experiments were approved by and performed in accordance with the guidelines of the Institutional Animal Care and Use Committee at the University of North Carolina (UNC). De-identified human tumour samples and informed consent were obtained from the patients by the UNC Tissue Procurement Facility under the protocol UNC-LCCC-9001. This study did not involve recruitment of patients or use of clinical data. No demographic identifiers were obtained for any of the patients, and their gene mutational information is provided in Supplementary Table 8. A cryopreserved specimen of an MLL-AF9^{+} AML PDX model was obtained from Public Repository of Xenografts (DFAM-68555, PRoXe; https://www.proxe.org).

Cells and tissue culture. The cell lines used in the study included 293T (American Tissue Culture Collection (ATCC), CRL-3216), HeLa (ATCC, CCL-2), MV4;11 (ATCC, CRL-9591), RS4;11 (ATCC, CRL-1873), MOLM-13 (Deutsche Sammlung von Mikroorganismen und Zellkulturen (DSMZ), ACC554), KOPN-8 (DSMZ, ACC552), EOL-1 (DSMZ, ACC386), K562 (ATCC, CRL-243) and THP-1 (ATCC, TIB-202). A MM1.S-derivative line with CRBN KO (*CRBN*$^{-/-}$) was provided by J. Brander and W. Kaelin (Dana Farber Cancer Institute). Luciferase-labelled cells were generated by infection with MSCV-luciferase-IRES-neo retrovirus and subsequent selection. Luciferase expression was validated using a luciferase assay system (Promega, E1500). MV4;11 cells stably expressed with doxycycline (Dox)-inducible Cas9 (iCas9)[61] were a gift from X. Shi and H. Wen (Van Andel Institute). The identity of cell lines was ensured by UNC's Tissue Culture Facility with genetic signature analyses, and examination of mycoplasma contamination was performed using commercial detection kits (Lonza, LT27-286).

Methods for cell transfection, generation of stable expression cell lines, assays for cell cycle progression, apoptosis and colony formation, as well as HSPC purification and related colony formation unit (CFU) assays are provided in Supplementary Note 1.

Plasmid construction. EZH2 or cMyc was fused with a Flag or a HA tag and cloned into the pcDNA-3.1 (Invitrogen) and pCDH-EF1-MCS-IRES-neo vector (System Biosciences). Serial deletion constructs of cMyc were generated by PCR and subcloned into pcDNA-3.1, and mutagenesis was performed using Site-Directed Mutagenesis kits (Agilent, 200521). Luciferase reporter assays for the TAD of EZH2 and VP16 (ref. [62]) were conducted after fusing to the DNA-binding domain of GAL4 in pCMX-GAL4-DBD. Recombinant protein was produced with bacterial expression systems of pGEX6P1 (GE Healthcare) or pET28a (EMD Biosciences). Primers used for cloning are listed in Supplementary Table 11.

ChIP-seq. ChIP-seq was performed using a chromatin crosslinking-based protocol[63–65]. Cells were collected and fixed with formaldehyde, followed by the addition of glycine to stop crosslinking. After washing, lysis and sonication of cells, a fixed fraction of *Drosophila melanogaster* chromatin was added as a spike-in control into the same amount of sonicated chromatin across all samples. Magnetic beads (Dynabeads M-280 sheep anti-rabbit IgG; Invitrogen, 11203D) pre-conjugated with specific antibodies against the target protein (anti-EZH2 (Cell Signaling Technology, 5246) or anti-H3K27me3 (Cell Signaling Technology, 9733)), together with those against H2Av (Active Motif, 39715, for the *Drosophila* spike-in chromatin), were added into samples for ChIP. After bead washing and elution, the eluted chromatin was de-crosslinked, followed by protein and RNA digestion and DNA purification. Multiplexed ChIP-seq libraries were prepared using a NEBNext Ultra II kit (NEB, E7103L) and sequenced on a Nextseq 500 system using a Nextseq 550 High Output kit v.2.5 (Illumina).

ChIP-seq data analysis. Reads were mapped to the human genome (hg19) and *Drosophila* genome (dm3) using BWA (v.0.7.12; default parameters)[66]. Unique reads mapped to a single best-matching location with no more than two mismatches were kept, which were then subjected to removal of PCR-caused read duplicates using Picard and Samtools. We filtered out reads with a mapping quality score of <20 for downstream analysis. MACS2 was used for peak identification with data from input as controls and default parameters[67]. Alignment files in the bam format were transformed into read coverage files (bigwig format) using DeepTools[68]. Scaling factors were calculated based on the spike-in (dm3) read count as previously described[69], and normalization was done using the bamCompare function of deeptools with a bin size of 10 and read length of 250. Profiles of ChIP-seq read densities are displayed in Integrative Genomics Viewer (IGV, Broad Institute). Heatmaps for ChIP-seq signals were generated using the deepTools computeMatrix and plotHeatmap functions. Distributions of peaks were analysed using the annotatePeaks.pl function of HOMER (hypergeometric optimization of motif enrichment)[70]. Motif analysis of EZH2-solo peaks was performed using the SeqPos tool in Cistrome to uncover the motifs that are enriched close to the peak centres by taking the peak locations as the input[71].

CUT&RUN and data analysis. CUT&RUN[34] was performed as previously described[65] with a commercial kit (EpiCypher CUTANA pAG-MNase for ChIC/CUT&RUN, 15-1116). One million cells were used for CUT&RUN, and 5 ng of the purified CUT&RUN DNA was used for construction of multiplexed libraries with a NEB Ultra II DNA Library Prep kit, followed by sequencing (using an Illumina NextSeq 500). Reads were mapped to hg19 using bowtie2.3.5. Non-primary alignment, PCR duplicates or blacklist regions were removed from aligned data using Samtools (v/1.9), Picard MarkDuplicates function (v.2.20.4) and bedtools (v.2.28.0), respectively. Peak calling was performed using MACS2 (macs2 callpeak -f BAMPE -g hs/mm –keep-dup 1). Deeptools (v.3.3.0) was used to generate bigwig files, heatmaps and averaged plots of signals. Genomic binding profiles were generated using deepTools bam-Compare functions.

Recombinant protein purification. For GST fusion recombinant protein expression, the transformed *Escherichia coli* BL21 bacterial cells were grown in the Luria–Bertani medium containing ampicillin (50 μg ml^{-1}, Amresco) at 37 °C overnight. Isopropyl-β-D-1-thiogalactopyranoside (IPTG, 0.2 mM, Sigma-Aldrich) was applied to induce protein expression when the OD_{600} reached 0.8. Bacterial pellets were then collected after induction at 37 °C for 5 h and disrupted by sonication. GST fusion protein was purified with the slurry of glutathione-sepharose beads (Pharmacia, 17-0756-01) and stored at 4 °C in buffer (25 mM Tris pH 7.5, 500 mM NaCl, 0.2 mM EDTA, 10% glycerol, 1 mM DTT, 1× protease inhibitor).

The pET28a plasmid containing His6×-tagged EZH2 or cMyc was transformed into the *E. coli* BL21(DE3) strain. LB medium with kanamycin was inoculated with the transformed bacteria cells, followed by protein expression induction with IPTG (0.4 mM) at an optical density of 2.8 and then grown overnight at 15 °C. For protein purification, bacteria cells were resuspended in a buffer (50 mM phosphate pH 7.5, 1 M NaCl, 5% glycerol, 1 mM PMSF), lysed by sonication and clarified by centrifugation at 18,000*g* for 1 h at 4 °C. The supernatant was applied to an automated affinity chromatography system (AKTA, GE Healthcare) with a Ni-NTA column (His-Trap HP, GE Healthcare) using buffer A (50 mM Tris pH 7.5, 250 mM NaCl) and buffer B (50 mM Tris pH 7.5, 250 mM NaCl, 250 mM imidazole). Additional purification was performed by size-exclusion chromatography on HiLoad Superdex 200 pg (26/600, GE Healthcare) equilibrated in 20 mM HEPES pH 7.4, 150 mM NaCl for EZH2-TAD and its mutant and 50 mM Tris-HCl pH 7.5, 150 mM NaCl, 5% glycerol for cMyc-CD.

For recombinant p300, His6×–p300 was expressed from pFastBac1 vector in High Five cells and purified on Ni-NTA beads in BC buffer (20 mM HEPES pH 7.9, 1 mM EDTA, 10% glycerol and 1 mM DTT) with 100 mM NaCl and 300 mM imidazole[72,73]. His6×–p300 was further purified on a Q sepharose column (HiTrap, GE Healthcare) in BC buffer and eluted between 100 and 600 mM NaCl. The purity of the protein preparation was assessed on gels, and the pure fractions (>90%) were collected and flash frozen until use.

Co-IP and GST pulldown. Cell pellets were lysed in EBC buffer (freshly supplemented with protease/phosphatase inhibitors) on ice for 30 min. After sonication, debris was removed by centrifugation at 12,000*g* for 15 min at 4 °C. A total of 1 mg of protein from lysate was incubated with antibodies at 4 °C, followed by the addition of 10 μl of protein A/G magnetic beads (Bio-Rad) and rotation for 3 h at 4 °C. To test the potential involvement of DNA/chromatin binding for protein–protein association, the cell lysate was pretreated with 250 U μl^{-1} of Benzonase nuclease (Sigma, E1014) for 1 h on ice, followed by IP in the presence of 10 mg ml^{-1} ethidium bromide (Invitrogen, 15585011) as previously described[74]. For IP of tagged protein, HA-conjugated (Roche, 11815016001) or Flag beads (Sigma, M8823) were incubated with lysate overnight at 4 °C. In vitro translated protein was generated using pCDNA3.1 plasmids and a TnT Quick Coupled Transcription/Translation system (Promega, L1170). GST pulldown was conducted with either cell lysate or the in vitro translated protein and 1 μg of GST fusion recombinant protein[75,76].

Gene knockdown and CRISPR–Cas9-mediated KO. Lentiviral short hairpin RNA (shRNA) plasmids for knockdown (KD) of *EZH2* (TRCN0000010475), *HUWE1* (TRCN0000073303 and TRCN0000073305) or *UBR5* (TRCN0000003409 and TRCN0000003412) were obtained from Sigma, and those targeting *FBW7* and *SKP2* were provided by Q. Zhang (UT Southwestern Medical Center), H.-K. Lin (Wake Forest University) and W. Wei (Harvard University)[77,78]. The E3 ligase FBW7 (ref. [79]), UBR5 (ref. [80]), SKP2 (ref. [81]) or HUWE1 (ref. [82]) can mediate cMyc degradation. shRNA targeting the 3′ untranslated region of *EZH2* was cloned into a Dox-inducible Tet-pLKO-puro vector (Addgene, 21915). Single guide RNAs (sgRNAs) targeting human *EZH2* or *cMyc* were designed using an online tool (http://chopchop.cbu.uib.no/) and cloned into pLenti-LRG-2.1-Neo (Addgene, 125593). A lentiviral plasmid that allows the Dox-inducible expression of SpCas9 was obtained from D. Sabatini. Methods for RT–qPCR are provided in Supplementary Note 1. Information for shRNA or sgRNA is listed in Supplementary Table 11.

RNA-seq and data analysis. Total RNA was first purified using a RNeasy Plus Mini kit (Qiagen, 74136) and then treated with a Turbo DNA-free kit (Thermo, AM1907) to remove genomic DNA. For spike-in controlled RNA-seq, equal amounts of ERCC RNA Spike-In Mix (Thermo, 4456740) was added into all RNA samples before library construction. Multiplexed RNA-seq libraries were subjected to deep-sequencing. Reads were mapped to the reference genome

followed by analysis of DEGs as previously described[63–65]. Fastq files were aligned to the GRCh38 human genome (GRCh38.d1.vd1.fa) using STAR (v.2.4.2)[83] with the following parameters: –outSAMtype BAM Unsorted–quantMode TranscriptomeSAM. Transcript abundance was estimated using salmon (v.0.1.19)[84] to quantify the transcriptome defined by Gencode v22. Gene level counts were summed across isoforms and genes with low counts (maximum expression < 10) were filtered for downstream analyses. Raw read counts were used for differential gene expression analysis by DESeq2 (v.1.38.2)[85], for which the size normalization factor was estimated based on either median-of-ratios or read counts of spike-in sequences. GSEA[86] was carried out using the GSEA software (v.4.1.0) for testing enrichment of Hallmark or curated gene sets (C2). Gene sets were obtained from the Molecular Signatures Database v.6.2 (MSigDB; https://www.broadinstitute.org/gsea/msigdb/index.jsp; C2 curated gene sets or C6 oncogenic signatures). Expression heatmaps were generated using mean-centred $\log_2$-converted transcripts per million (TPM) sorted in descending order based on expression values in the R package gplots v.3.0.3 with either no clustering or column hierarchical clustering by average linkage. Volcano plots visualizing DEGs were produced using the R package EnhancedVolcano v.3.11. Annotation of DEGs was conducted using either database for annotation, visualization and integrated discovery (DAVID; v.6.8)[87] and Metascape[88]. DisGeNET[89] was used to annotate genes associated with human disease. BETA analysis was used to define direct target genes by integrating ChIP-seq peaks with DEG data[90].

Immunoblotting, signal quantification and protein half-life measurement. Cells were lysed in EBC buffer (50 mM Tris pH 8.0, 120 mM NaCl, 0.5% NP40, 0.1 mM EDTA and 10% glycerol) freshly supplemented with protease/phosphatase inhibitors (Roche). Protein concentration was measured by Bradford assay (Bio-Rad). Equal amounts of protein lysate were used for immunoblotting. To measure the stability and half-life of the protein in cells, we treated cells with 0.1 mg ml^{-1} cycloheximide (CHX; a protein synthesis inhibitor) and collected cell samples at different time points of CHX treatment, followed by immunoblotting of target protein using total cell lysate. Protein degradation curves were generated as previously described[91]. Quantification of immunoblotting signals was performed by normalizing to tubulin or GAPDH signals with ImageJ. Antibody information is provided in Supplementary Table 12.

Luciferase reporter assay. Cells, seeded in 24-well plates, were co-transfected with plasmids of GAL4-DBD-fusion, a luciferase reporter pGL2-5×GAL4-SV40 (Promega) and an internal control (pRL-CMV-Renilla). At 48 h after transfections, luciferase activity was measured using a Dual Luciferase Reporter Assay system (Promega, E1910). Data were normalized to Renilla luciferase.

ITC. Direct binding between EZH2-TAD and cMyc-CD was analysed using a MicroCal iTC200 (Malvern) in 100 mM Tris-HCl pH 7.5 plus 150 mM NaCl at 25 °C. After an initial 0.4 µl injection, 13 injections from the syringe solution (500 µM of EZH2-TAD) were titrated into 300 µl of the protein solution (50 µM of cMyc-CD) in the cell, which was stirred at 1,000*g*. The data were fitted using a single-binding-site model using Microcal Origin 7.0 (Malvern). The reported values represent the mean ± s.d. from three independent measurements.

Chemicals. The synthesis and characterization of MS177, MS177N1 and MS177N2 are described in Supplementary Note 1. Pomalidomide (36471) was purchased from AstaTech. GSK126 (S7061), EPZ6438 (S7128), MLN4924 (S7109) and A-485 (S8740) were purchased from Selleck Chemical. CPI-1205 and UNC1999 were synthesized as previously reported[15,17]. EPZ-6438 (refs. [12,13]), GSK126 (ref. [14]), UNC1999 (ref. [15]), C24 (ref. [16]) and CPI-1205 (ref. [17]), A-485 (ref. [46]), UNC6852 (ref. [45]) (kindly provided by L. James, UNC at Chapel Hill) and UNC7043 (ref. [45]) were used as previously described.

EZH2 methyltransferase inhibition assay. In vitro EZH2 methyltransferase assays, performed in duplicate (by Reaction Biology), monitors the transfer of a tritium(^{3}H)-labelled-methyl group from *S*-adenosyl methionine (SAM) to histone. A total of 5 nM of the recombinant five-component PRC2 (comprising EZH2, EED, SUZ12, RBAP48 and AEBP2) was used as the enzyme, 0.05 µM of core histone as the substrate and 1 µM of SAM as the methyl donor.

Compound selectivity. Assays for determining the selectivity of MS177 against 23 other methyltransferases (performed by Reaction Biology) used the same ^{3}H-labelled SAM assay as described above, with assays against EZH1 performed in duplicate at the indicated compound concentrations and those against other methyltransferases performed in duplicate at 10 µM. The selectivity of MS177 against a panel of kinases, performed in duplicate by Eurofins Cerep, was tested at 10 µM, with the effectiveness of the compound calculated as the percentage of inhibition relative to mock-controlled activity. The selectivity of MS177 against a panel of 45 GPCRs, ion channels and transporters was assayed at 10 µM in quadruplicate by the NIMH-PDSP (http://pdsp.med.unc.edu/) using radioligand binding assays (per target).

Cell growth inhibition. Cells, seeded in triplicate in each well of 24-well plates, were subjected to treatment of compounds at various concentrations. Medium containing fresh compound was changed every 2 days. Flow-growing cell cultures were periodically diluted to keep the density at less than 1×10^6 cells per ml. Cell counting was conducted using an automated TC10 counter (Bio-Rad) every 2 days. EC_{50} values were calculated as previously described[18] using a nonlinear regression analysis of the mean ± s.d. from triplicate datasets for each biological assay.

Culture of primary AML cells from patients. Cryopreserved primary mononuclear cells of de-identified patients with AML (from bone marrow) were obtained from the UNC's Tissue Procurement Core Facility and cultivated on a layer of HS27 stromal cells (ATCC, CRL-1634). In brief, HS27 cells were first expanded in medium (DMEM base medium,10% FBS, 1% antibiotics), irradiated at 15 Gray and plated at a confluent density. Cryopreserved AML cells were quickly thawed, resuspended in PBS with 5% BSA and 8% Dextran-40, collected by centrifugation at 500*g* for 5 min and then resuspended in DMEM supplemented with 15% FBS, 50 µM β-mercaptoethanol, 1% antibiotics, 2 mM L-glutamine and a human cytokine cocktail comprising 100 ng ml^{-1} stem cell factor, 10 ng ml^{-1} IL-3, 20 ng ml^{-1} IL-6, 10 ng ml^{-1} thrombopoietin and 10 ng ml^{-1} FLT3 ligand (Peprotech), followed by plating onto the layer of irradiated HS27 cells and co-culture at 37 °C. In vitro expansion of primary AML samples was monitored by tryptophan blue staining.

Cell fractionation. Cells were collected, washed with cold PBS and resuspended in 200 µl of CSK buffer (10 mM PIPES pH 7.0, 300 mM sucrose, 100 mM NaCl, 3 mM $MgCl_2$, 0.1% Triton X-100, freshly supplemented with protease/phosphatase inhibitor cocktail), followed by incubation on ice for 30 min[64,65]. Then, the sample was subject to centrifugation at 1,300*g* for 5 min at 4 °C to collect supernatant (which contains soluble proteins) and pellet fractions (which contains the chromatin-associated proteins). Cell pellets were dissolved in 1.5× SDS loading buffer. The same amounts of protein sample were used for immunoblotting.

Ubiquitination assay. Cells were collected and extracted in 100 µl of EBC buffer containing 1% SDS. Cell extracts were heat-denatured at 95 °C for 5 min and diluted with 900 µl of EBC buffer. After sonication and centrifugation, lysates were subjected to IP with antibodies of target proteins, followed by anti-ubiquitin immunoblotting.

Complete blood counting. Blood samples from mice were collected in heparin tubes on day 5, 10, 15 and 21 by tail nick and counted using a Hemavet 950FS machine (Drew Scientific).

In vivo pharmacokinetics studies. Male Swiss albino mice ($n = 6$) were dosed at 50 mg per kg body weight via i.p. injection. Blood samples were collected into microtubes containing 20% K_2EDTA solution as an anticoagulant under light isoflurane anaesthesia from three mice at 0.5, 1, 2, 4, 8 and 12 h. Plasma was immediately collected from blood by centrifugation at 4,000*g* for 10 min at 4 °C and stored below −80 °C until bioanalysis. Concentrations of MS177 in plasma were determined by a fit-for-purpose liquid chromatography with tandem mass spectrometry (LC–MS/MS) method. The non-compartmental-analysis tool of Phoenix WinNonlin (v.6.3) was used to assess pharmacokinetics parameters. Peak plasma concentration (C_{max}) and time to peak plasma concentration (T_{max}) were the observed values.

PDX models. NOD-SCID IL2Rg^{null}-3/GM/SF mice (NSG-SGM3) and NOD/SCID/IL2Rgamma^{null} (NSG) mice were acquired from The Jackson Laboratory. Mice were housed in a germ-free environment with food and tap water ad libitum. Room temperature and relative humidity were held at 22 ± 2 °C and 30–70%, respectively. Automatic light control guaranteed a 12-h light/dark cycle (7:00 to 19:00/19:00 to 7:00). PDX cells were stably transfected with eGFP/Firefly-luciferase (FFLuc) genes[92]. The eGFP/FFLuc-transduced cells were injected into NSG-SGM3 mice (8-week-old females) via tail vein, expanded and collected from spleen via sorting for GFP$^+$/hCD33$^+$ cells (FACSAria-II; BD Biosciences). Approximately 0.2 million of GFP$^+$/hCD33$^+$ PDX cells were then injected into each one of a second set of NSG-SGM3 mice for further expansion. Seven weeks later, cells were collected from spleens of leukaemic mice and then frozen in liquid nitrogen until use or immediately used for xenograft assays.

In vivo dosing. MS177 was dissolved in 5% *N*-methyl-2-pyrrolidone, 5% Solutol HS-15, 60% captisol (20% w/v) and 30% PEG-400. For generating subcutaneous (s.c.) xenograft models, cells (5 million for RS4;11 or PDX cells or 2 million for EOL-1 cells) were suspended in 100 µl of a 1:1 mixture of DPBS and Matrigel (Corning) and then injected subcutaneously into the bilateral flank of 8-week-old female NSG (used for human cell line xenograft) or NSG-SGM3 mice (used for PDX). The tumour volume (mm^3) was defined using the formula of (length × width^2)/2, where length and width represent the largest and perpendicular tumour diameter, respectively. The tumour volume was measured three times per week with electronic calipers. Once the s.c. tumours reached an average of 50–100 mm^3, animals were randomized so that the average tumour volume at the beginning of treatment was uniform across all groups. Dosing of MS177 (i.p.) was either 100 mg per kg BID for 6 days (Monday to Saturday) per

week or 200 mg per kg BID for 3 days (Monday, Wednesday and Friday) per week. For orthotopic xenograft models, 0.2 million of the luciferase-labelled PDX cells were injected intravenously (i.v.) to each one of NSG-SGM3 mice. Tumour growth was monitored via weekly chemiluminescence imaging of live mice following the i.p. injection with D-luciferin. Once tumours reached an average bioluminescence imaging (BLI) signal of 1×10^5 photons s^{-1}, animals were randomized so that the average BLI signal at the beginning of treatment was same across all groups, which were subjected to dosing as described above. Mice were monitored daily (UNC's Animal Studies Core), with body weight and tumour growth (tumour volume or BLI signals) measured two to three times per week to avoid reaching maximal tumour size/burden. Investigators were blinded to the allocation of mice and outcome assessment (conducted by UNC's Animal Studies Core).

Intratumour and intraplasma drug concentration analysis. NSG mice were treated with 200 mg per kg of MS177 (i.p.) BID for 5 days. On day 5, mice were euthanized 2 h after the last treatment. For plasma preparation, 200 µL of blood was collected in EDTA-treated tubes and centrifuged at 2,000*g* for 10 min at 4 °C to collect the supernatant (stored at −20 °C until use). The s.c. tumours, collected immediately after animals were euthanized, were cut into pieces, snap-frozen in liquid nitrogen and stored at −20 °C. Tumour samples were homogenized in 80:20 (v/v) water:acetonitrile at a 1:9 (w/v) ratio, diluted by fivefold, and analysed against plasma calibration curves. MS177 concentrations in plasma and tumour samples were analysed by LC–MS. A Waters UPLC BEH C18 column (2.1 × 50 mm, 1.7 µm) was used for LC. Mobile phase A consisted of 95:5:0.1 (v/v/v) water:acetonitrile:formic acid. Mobile phase B consisted of 50:50:0.1 (v/v/v) methanol:acetonitrile:formic acid. An API 6500 was used for MS/MS analysis. Electrospray was used for the ionization method (positive ion).

Statistics and reproducibility. Statistical analyses were performed using GraphPad Prism (v.9). Unpaired two-tailed Student's *t*-test was used for experiments comparing two sets of data with assumed normal distribution. For comparisons of tumour growth, two-way analysis of variance was used. Kaplan–Meier survival curves were statistically analysed using log-rank (Mantel–Cox) test. Data are presented as the mean ± s.d. from at least three independent experiments. *P* values are denoted as follows: $^*P < 0.05$, $^{**}P < 0.01$ and $^{***}P < 0.005$. $P < 0.05$ was considered to be statistically significant. NS denotes not significant. No statistical methods were used to predetermine sample sizes. All data from representative experiments (such as imaging and micrographs) were repeated at least two times independently with similar results obtained.

Reporting Summary. Further information on research design is available in the Nature Research Reporting Summary linked to this article.

Data availability

The genomic dataset of this study, including ChIP-seq, CUT&RUN and RNA-seq, have been deposited in NCBI Gene Expression Omnibus (GEO) database under accession code GSE180448. Human AML datasets were derived from TCGA Research Network (http://cancergenome.nih.gov/). Publicly available datasets used in this work were from NCBI GEO accession numbers GSE113042 (ChIP-seq of H3K4me3, H3K27ac, SMARCA4 and SMARCC1 in EOL-1 cells), GSE82116 (ChIP-seq of H3K27ac, H3K9ac and POL2 in MV4;11 cells), GSE73528 (ChIP-seq of MLLn and MLLc in MV4;11 cells), GSE101821 (ChIP-seq of BRD4 in MV4;11 cells), GSE29611 (ChIP-seq of EZH2 and H3K27me3 in GM12878, HUVEC and K562 cells, as well as SUZ12 in K562 cells), GSE30226 (ChIP-seq of cMyc in HUVEC and K562 cells) and GSE33213 (ChIP-seq of cMyc in GM12878 cells). Other data supporting the findings of this study are available upon request. Source data are provided with this paper.

Code availability

We did not use custom code. All software and packages used in this study are listed in Nature Research Reporting Summary and are publicly available.

References

61. Wan, L. et al. ENL links histone acetylation to oncogenic gene expression in acute myeloid leukaemia. *Nature* **543**, 265–269 (2017).
62. Wang, G. G., Pasillas, M. P. & Kamps, M. P. Persistent transactivation by Meis1 replaces Hox function in myeloid leukemogenesis models: evidence for co-occupancy of Meis1–Pbx and Hox–Pbx complexes on promoters of leukemia-associated genes. *Mol. Cell. Biol.* **26**, 3902–3916 (2006).
63. Cai, L. et al. ZFX mediates mon-canonical oncogenic functions of the androgen receptor splice variant 7 in castrate-resistant prostate cancer. *Mol. Cell* **72**, 341–354.e6 (2018).
64. Yu, X. et al. A selective WDR5 degrader inhibits acute myeloid leukemia in patient-derived mouse models. *Sci. Transl. Med.* **13**, eabj1578 (2021).
65. Li, J. et al. ZMYND11–MBTD1 induces leukemogenesis through hijacking NuA4/TIP60 acetyltransferase complex and a PWWP-mediated chromatin association mechanism. *Nat. Commun.* **12**, 1045 (2021).
66. Li, H. & Durbin, R. Fast and accurate long-read alignment with Burrows–Wheeler transform. *Bioinformatics* **26**, 589–595 (2010).
67. Zhang, Y. et al. Model-based analysis of ChIP-seq (MACS). *Genome Biol.* **9**, R137 (2008).
68. Ramirez, F. et al. deepTools2: a next generation web server for deep-sequencing data analysis. *Nucleic Acids Res.* **44**, W160–W165 (2016).
69. Ahn, J. H. et al. Phase separation drives aberrant chromatin looping and cancer development. *Nature* **595**, 591–595 (2021).
70. Heinz, S. et al. Simple combinations of lineage-determining transcription factors prime *cis*-regulatory elements required for macrophage and B cell identities. *Mol. Cell* **38**, 576–589 (2010).
71. Liu, T. et al. Cistrome: an integrative platform for transcriptional regulation studies. *Genome Biol.* **12**, R83 (2011).
72. An, W., Kim, J. & Roeder, R. G. Ordered cooperative functions of PRMT1, p300, and CARM1 in transcriptional activation by p53. *Cell* **117**, 735–748 (2004).
73. Shimada, M. et al. Gene-specific H1 eviction through a transcriptional activator→p300→NAP1→H1 pathway. *Mol. Cell* **74**, 268–283.e265 (2019).
74. Lu, H. et al. RECQL4 promotes DNA end resection in repair of DNA double-strand breaks. *Cell Rep.* **16**, 161–173 (2016).
75. Liu, X. et al. Genome-wide screening identifies SFMBT1 as an oncogenic driver in cancer with VHL loss. *Mol. Cell* **77**, 1294–1306.e5 (2020).
76. Cai, L. et al. An H3K36 methylation-engaging Tudor motif of Polycomb-like proteins mediates PRC2 complex targeting. *Mol. Cell* **49**, 571–582 (2013).
77. Inuzuka, H. et al. SCF^{FBW7} regulates cellular apoptosis by targeting MCL1 for ubiquitylation and destruction. *Nature* **471**, 104–109 (2011).
78. Inuzuka, H. et al. Acetylation-dependent regulation of Skp2 function. *Cell* **150**, 179–193 (2012).
79. King, B. et al. The ubiquitin ligase FBXW7 modulates leukemia-initiating cell activity by regulating MYC stability. *Cell* **153**, 1552–1566 (2013).
80. Qiao, X. et al. UBR5 is coamplified with MYC in breast tumors and encodes an ubiquitin ligase that limits MYC-dependent apoptosis. *Cancer Res.* **80**, 1414–1427 (2020).
81. Kim, S. Y., Herbst, A., Tworkowski, K. A., Salghetti, S. E. & Tansey, W. P. Skp2 regulates Myc protein stability and activity. *Mol. Cell* **11**, 1177–1188 (2003).
82. Myant, K. B. et al. HUWE1 is a critical colonic tumour suppressor gene that prevents MYC signalling, DNA damage accumulation and tumour initiation. *EMBO Mol. Med.* **9**, 181–197 (2017).
83. Dobin, A. et al. STAR: ultrafast universal RNA-seq aligner. *Bioinformatics* **29**, 15–21 (2013).
84. Patro, R., Duggal, G., Love, M. I., Irizarry, R. A. & Kingsford, C. Salmon provides fast and bias-aware quantification of transcript expression. *Nat. Methods* **14**, 417–419 (2017).
85. Love, M. I., Huber, W. & Anders, S. Moderated estimation of fold change and dispersion for RNA-seq data with DESeq2. *Genome Biol.* **15**, 550 (2014).
86. Subramanian, A. et al. Gene set enrichment analysis: a knowledge-based approach for interpreting genome-wide expression profiles. *Proc. Natl Acad. Sci. USA* **102**, 15545–15550 (2005).
87. Huang da, W., Sherman, B. T. & Lempicki, R. A. Systematic and integrative analysis of large gene lists using DAVID bioinformatics resources. *Nat. Protoc.* **4**, 44–57 (2009).
88. Zhou, Y. et al. Metascape provides a biologist-oriented resource for the analysis of systems-level datasets. *Nat. Commun.* **10**, 1523 (2019).
89. Pinero, J. et al. DisGeNET: a comprehensive platform integrating information on human disease-associated genes and variants. *Nucleic Acids Res.* **45**, D833–D839 (2017).
90. Wang, S. et al. Target analysis by integration of transcriptome and ChIP-seq data with BETA. *Nat. Protoc.* **8**, 2502–2515 (2013).
91. Liu, X. J. et al. Human cytomegalovirus IE1 downregulates Hes1 in neural progenitor cells as a potential E3 ubiquitin ligase. *PLoS Pathog.* **13**, e1006542 (2017).
92. Vera, J. et al. T lymphocytes redirected against the kappa light chain of human immunoglobulin efficiently kill mature B lymphocyte-derived malignant cells. *Blood* **108**, 3890–3897 (2006).

Acknowledgements

We thank members of the Wang and Jin laboratories, H. Uryu and K. Suzuki for technical support and helpful discussions; X. Shi, H. Wen, E. Lichtman, P. Armistead, H. Huang, J. Bradner, W. Kaelin, E. Guccione, S. Frye, L. James, A. Chinnaiyan, H. Lin, W. Wei and Q. Zhang for providing reagents and cell lines; staff at the National Institute of Mental Health Psychoactive Drug Screening Program (NIMH-PDSP) for generating the selectivity data of MS177 over GPCRs, ion channels and transporters; staff at the UNC's core facilities, including the Imaging Core, the High-throughput Sequencing Facility (HTSF), the Bioinformatics Core, the Flow Cytometry Core, the Tissue Culture Facility, the Tissue Procurement Facility and the Animal Studies Core, for their professional assistance of this work. The cores affiliated to the UNC Cancer Center are

supported in part by the UNC Lineberger Comprehensive Cancer Center Core Support Grant P30-CA016086. This work was supported in part by R01CA218600 (to J.J. and G.G.W.), R01CA268519 (to G.G.W. and J.J.), R01CA211336 (to G.G.W.), R01CA215284 (to G.G.W.), R01CA230854 (to J.J.) and R01GM122749 (to J.J.) grants from the US National Institutes of Health; a Kimmel Scholar Award (to G.G.W.); Gabrielle's Angel Foundation for Cancer Research (to G.G.W.); When Everyone Survives (WES) Leukemia Research Foundation (to G.G.W.); and UNC Lineberger Cancer Center UCRF Stimulus Initiative grants (to G.G.W. and L.C.). G.G.W. is an American Cancer Society (ACS) Research Scholar, a Leukemia and Lymphoma Society (LLS) Scholar, and an American Society of Hematology (ASH) Scholar in Basic Science. This work utilized the NMR Spectrometer Systems at Mount Sinai acquired with funding from National Institutes of Health SIG grants 1S10OD025132 and 1S10OD028504.

Author contributions

J.W., X.Y., X.L., K.-S.P., A.M., Y.S., W.-C.P., D.F.A., T.O., W.-Y.C., J.L. and L.C. performed experiments. J.W. performed functional studies (including ChIP-seq, RNA-seq and CUT&RUN, as well as cancer biology works) and data analyses (under the direction of G.G.W.). X.Y. performed chemical biology studies (under the direction of J.J.). W.G. and Y-H.T. performed RNA-seq data analysis (under the direction of G.G.W. and L.C.). X.Y., A.M., J.L. and J.J. analysed the structure–activity relationship results. K.-S.P., T.O., W.-C.P. and J.W. conducted EZH2-TAD and protein complex characterizations (under the direction of J.J., W.-Y.C., R.G.R. and G.G.W.). J.J. and G.G.W. conceived the project, organized and led the study. J.W., X.Y., J.J. and G.G.W. wrote the manuscript with input from all authors.

Competing interests

Icahn School of Medicine at Mount Sinai filed a patent application (WO 2018/081530 A1) covering EZH2 degraders that lists J.J. and A.M. as inventors. The Jin Laboratory received research funds from Celgene Corporation, Levo Therapeutics, Cullgen, Inc. and Cullinan Oncology. J.J. is a co-founder, scientific advisory board member and equity shareholder in Cullgen Inc., and is a consultant for Cullgen Inc., EpiCypher Inc. and Accent Therapeutics Inc. The remaining authors declare no competing interests.

Additional information

Extended data is available for this paper at https://doi.org/10.1038/s41556-022-00850-x.

Supplementary information The online version contains supplementary material available at https://doi.org/10.1038/s41556-022-00850-x.

Correspondence and requests for materials should be addressed to Jian Jin or Gang Greg Wang.

Peer review information *Nature Cell Biology* thanks Martin Eilers, Thomas Milne and the other, anonymous, reviewer(s) for their contribution to the peer review of this work.

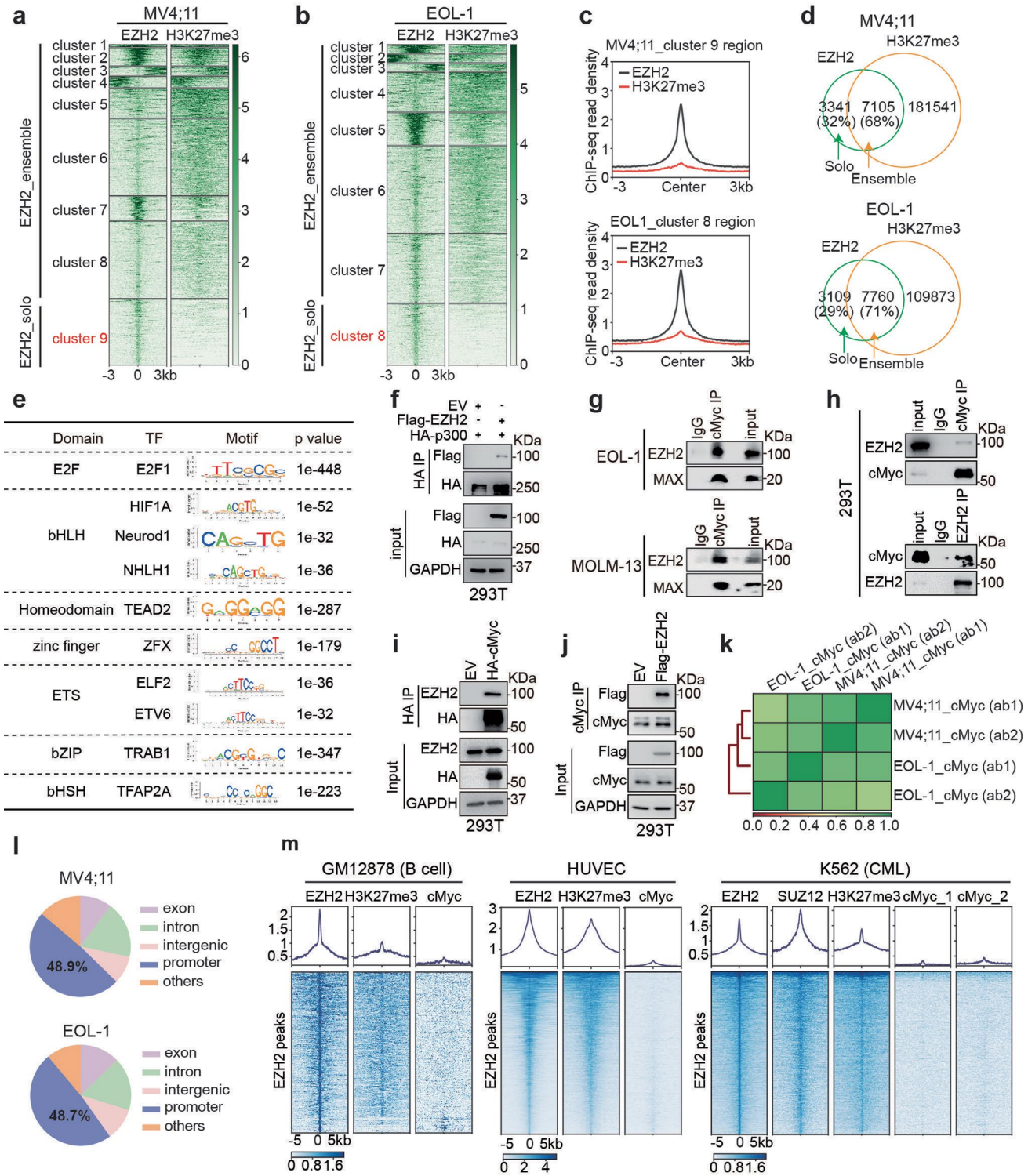

Extended Data Fig. 1 | See next page for caption.

Extended Data Fig. 1 | In MLL-rearranged (MLL-r) acute leukaemia, EZH2 exhibits the noncanonical 'solo'-binding pattern at sites enriched for the gene-activation-related histone marks and co-binding of RNA polymerase II (Pol II), (co)activators and cMyc, in addition to its canonical EZH2:PRC2 sites showing H3K27me3 co-binding. (a-b) Heatmaps showing the K-means clustered EZH2 and H3K27me3 ChIP-seq signal intensities ± 3 kb around peak centers in MV4;11 (a) and EOL-1 (b) cells. EZH2-'solo' and EZH2-'ensemble' refer to noncanonical EZH2 + /H3K27me3- peaks (cluster 9 in MV4;11 and cluster 8 in EOL-1 cells) and canonical EZH2 + /H3K27me3+ ones (clusters 1-8 in MV4;11 and clusters 1-7 in EOL-1 cells), respectively. (c) Averaged EZH2 and H3K27me3 ChIP-seq signals around ± 3 kb from the centers of the EZH2-'solo'-binding peaks in MV4;11 (top) and EOL-1 (bottom) cells. (d) Venn diagram showing the overlap between the called EZH2 and H3K27me3 peaks in MV4;11 (top) and EOL-1 (bottom) cells. (e) Motif search analysis of the EZH2-'solo'-binding peaks in MV4;11 cells by using the SeqPos tool in Cistrome. (f) Co-immunoprecipitation (co-IP) using anti-HA antibodies for assaying interaction between Flag-EZH2 and HA-p300 in 293 T cells. (g) Co-IP for endogenous EZH2 and MAX using anti-cMyc antibody in EOL-1 or MOLM-13 cells after the treatment of benzonase and ethidium bromide. (h) Co-IP for interaction between endogenous cMyc and EZH2 in 293 T cells by using either anti-cMyc (upper) or anti-EZH2 (bottom) antibodies. (i) Co-IP using anti-HA antibodies for interaction between endogenous EZH2 and the transiently expressed HA-cMyc in 293 T cells. (j) Co-IP using anti-cMyc antibodies for interaction between the transiently expressed Flag-EZH2 and endogenous cMyc in 293 T cells. (k) Pearson correlation analysis of cMyc ChIP-seq profiles generated by using two independent anti-cMyc antibodies in MV4;11 and EOL-1 cells. (l) Pie-chart plot showing the genomic distribution of peaks with both EZH2-'solo'-binding and cMyc-binding in MV4;11 (top) or EOL-1 (bottom) cells. (m) Heatmaps of EZH2, SUZ12, H3K27me3 and cMyc ChIP-seq signal intensities ± 5 kb from the centers of the called EZH2 peaks in the GM12878 lymphoblast cells (left), human umbilical vein endothelial cells (HUVEC; middle) and K562 chronic myeloid leukaemia (CML) cells (right).

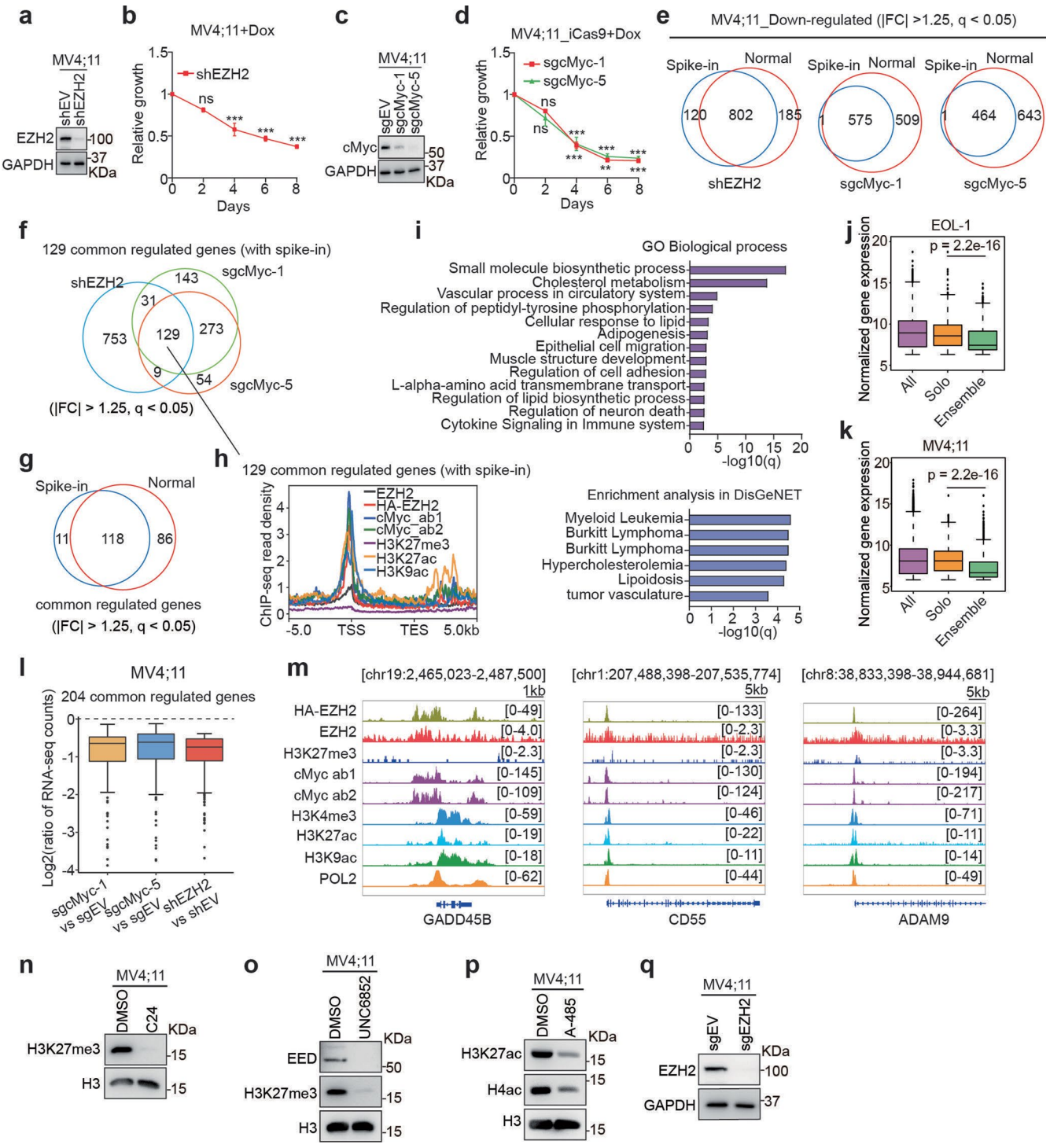

Extended Data Fig. 2 | See next page for caption.

Extended Data Fig. 2 | Cooperative recruitment of EZH2 and cMyc to common targets leads to gene activation in leukaemia. (a-d) Immunoblotting for EZH2 (a) or cMyc (c) and growth of MV4;11 cells following the doxycycline (Dox)-induced EZH2 knockdown (KD; shEZH2, b) or cMyc knockout (KO; by either sgcMyc-1 or sgcMyc-5, d), relative to respective empty vector (EV) controls. Y-axis shows growth after normalization to controls (n = 3; mean ± SD; unpaired two-tailed Student's t-test). iCas9, Dox-inducible Cas9. (e) Venn diagram using downregulated DEGs, identified by RNA-seq with (blue) or without (red) the spike-in control normalization, in MV4;11 cells following EZH2 KD or cMyc KO. (f) Venn diagram using downregulated DEGs, identified by RNA-seq with spike-in control normalization, in MV4;11 cells post-depletion of EZH2 or cMyc. (g) Venn diagram using the EZH2/cMyc co-upregulated genes, identified by RNA-seq with (blue) or without (red) spike-in control normalization, in MV4;11 cells. (h) Averaged signals of the indicated protein bound at the EZH2/cMyc co-upregulated genes (n = 129; shown in f). TSS, transcriptional start site; TES, transcriptional end site. (i) Gene Ontology (GO) analysis (top) and enrichment of the DisGeNet category (bottom) using the EZH2/cMyc co-upregulated genes in f. (j-k) Box plot showing overall expression of all genes (left) and those associated with EZH2-'solo' (middle) or -'ensemble' (right) peaks in EOL-1 (j) or MV4;11 (k) cells. The boundaries of box plots indicate the 25th and 75th percentiles, the center line indicates the median, and the whiskers (dashed) indicate 1.5× the interquartile range. Paired two-sided t-test. (l) Box plots showing log2-converted ratios for the indicated sample comparisons by using the 204 genes identified in main Fig. 2a. Box plot was defined the same as above. (m) IGV views of the indicated factor at GADD45B, CD55 and ADAM9 in MV4;11 cells. (n-p) Immunoblotting of the indicated protein in MV4;11 cells post-treatment with C24 (n), UNC6852 (o) or A-485 (p) for 24 hours. (q) EZH2 immunoblot following EZH2 KO. *, **, and *** denote $P < 0.05$, 0.01 and 0.005, respectively. NS denotes not significant. Numerical source data, statistics, exact P values and unprocessed blots are available as source data.

a

The 9aaTAD prediction result for the EZH2 trans-activating region

	sequence	start	end	C1	C2	C3	C4	C5	C6	C7	C8	C9	C10	C11	C12	= Rules for amino acid clustering
TAD1:	GTFIEELIK	143	151	+	+	+	+	+	+	+	+	+	+	+	+	perfect match
TAD2:	EIFVELVNA	169	177	+	+	+	+	+	+	+	+	+	+	+	+	perfect match

b

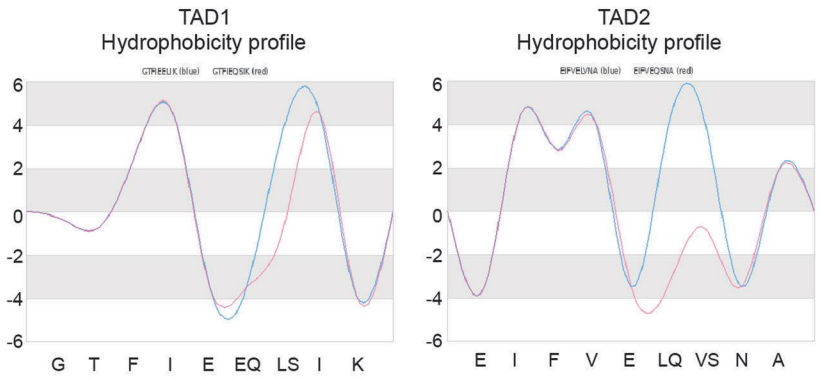

c

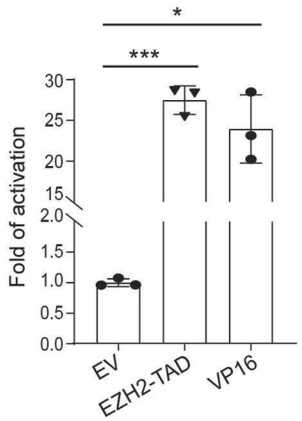

Extended Data Fig. 3 | A cryptic transactivation domain (TAD) of EZH2 (EZH2-TAD) directly associates with cMyc and coactivator (p300), promoting malignant growth of leukaemia cells. (a) Analysis with a prediction software, 9aaTAD, showing two putative TAD sequences (TAD1 and TAD2) within EZH2. Algorithm for the 9aaTAD amino acid pattern was applied in the search, and region clustering conformity was assessed by percentage. (b) Hydrophobicity profile of EZH2-TAD. (c) Luciferase reporter assay using the Gal4 DNA-binding domain (DBD) fusion of EZH2-TAD or VP16-TAD (a potent TAD as a positive control), compared to EV. Y-axis shows relative reporter activation after normalization of signals from an internal control (Renilla luciferase) and then to those of EV-transduced mock ($n = 3$; mean ± SD; unpaired two-tailed Student's t-test). *, **, and *** denote the P value of < 0.05, 0.01 and 0.005, respectively. NS denotes not significant. Numerical source data, statistics and exact P values are available as source data.

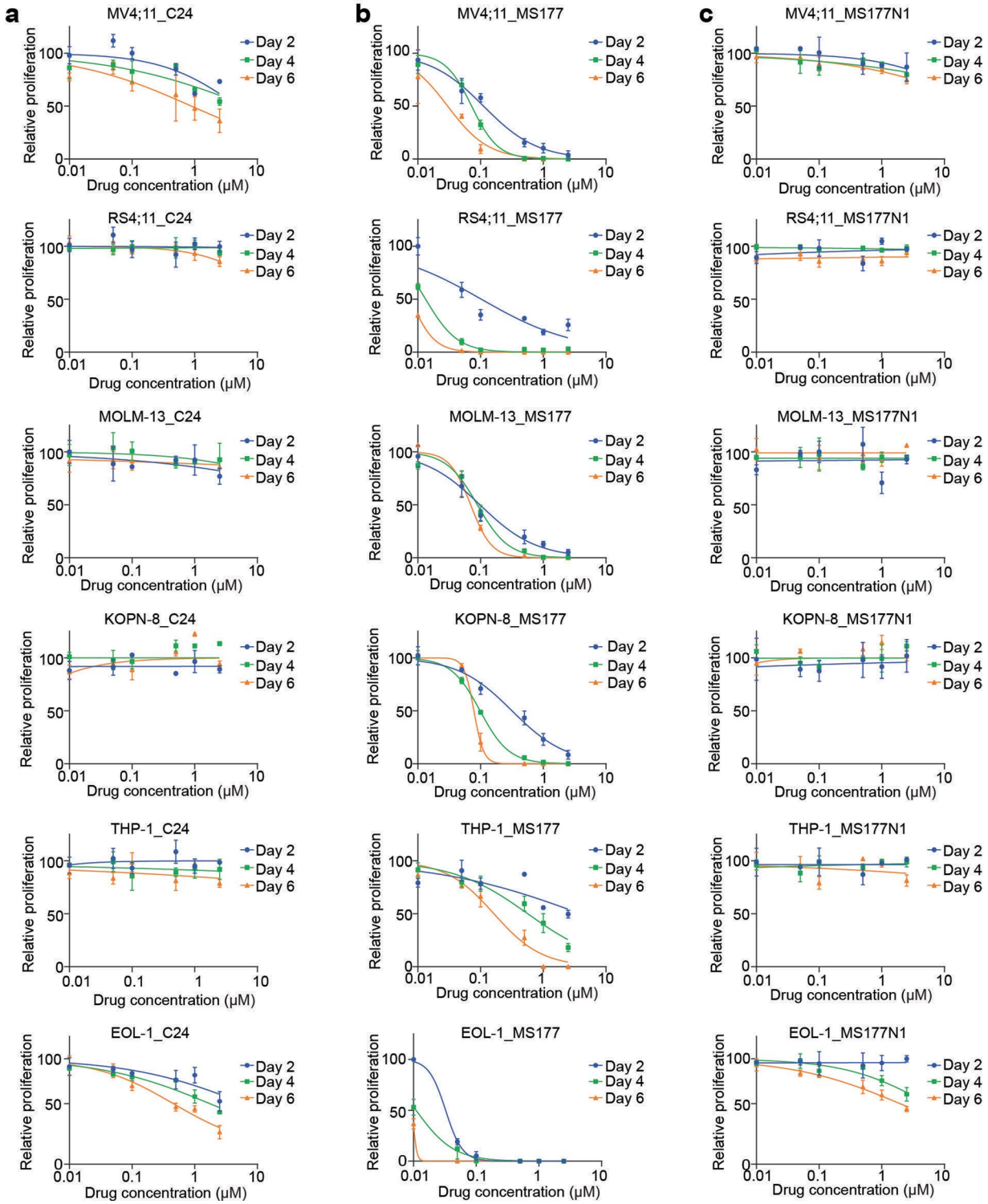

Extended Data Fig. 4 | Compared to C24 or MS177N1, MS177 is much more potent in inhibiting tumor cell growth. (a-c) Plots showing the growth inhibitory effect of various used concentrations (x-axis; in the log10 converted values) of either C24 (a), MS177 (b) or MS177N1 (c) using a panel of six MLL-r acute leukaemia cell lines (that is, MV4;11, RS4;11, MOLM-13, KOPN-8, THP-1 and EOL-1 cells), treated for 2, 4 or 6 days. Y-axis shows relative cell growth after normalization to DMSO-treated controls (n = 3; mean ± SD).

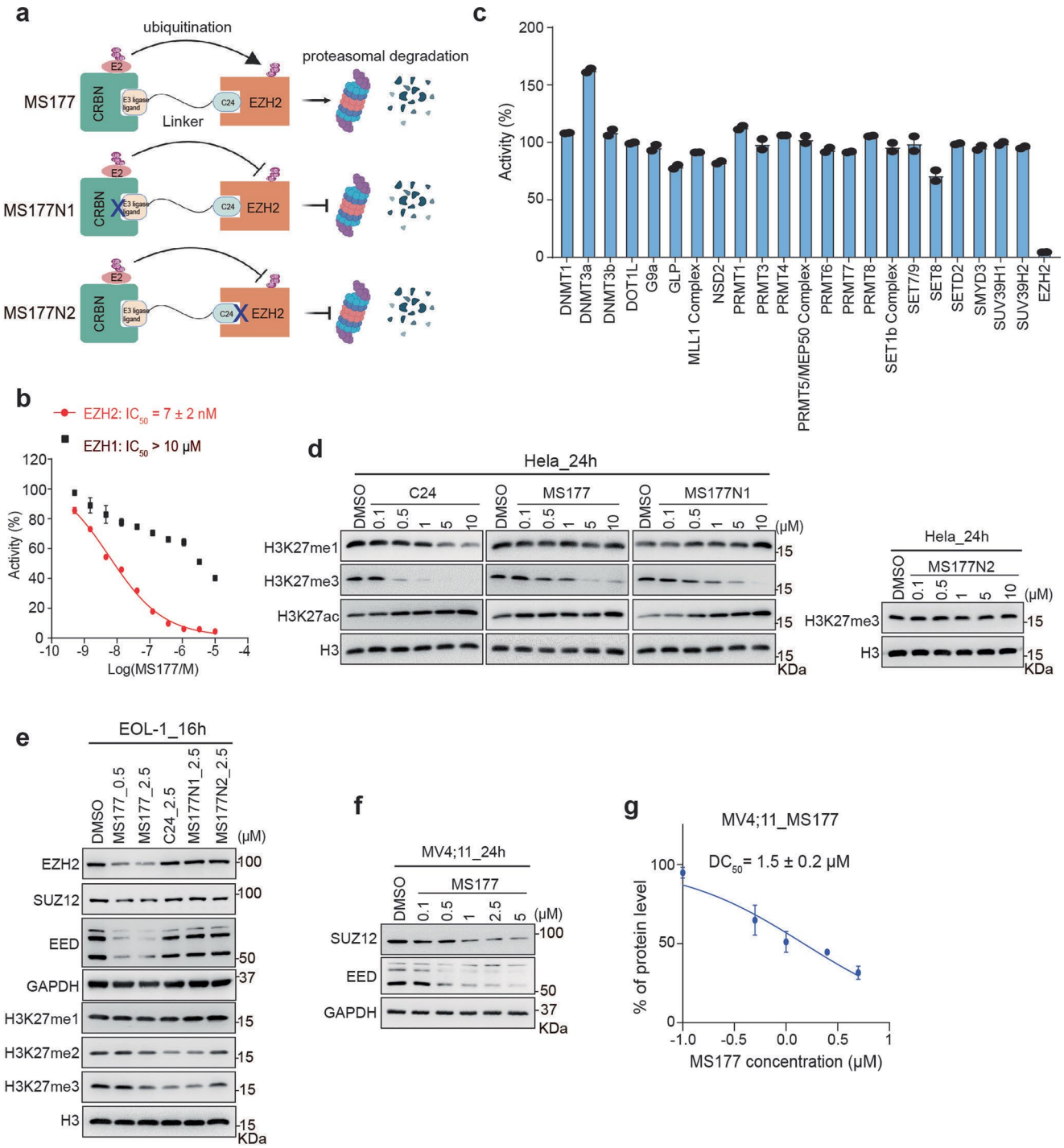

Extended Data Fig. 5 | Biochemical characterization of the EZH2-targeting PROTAC degrader, MS177. (a) Scheme showing the expected effect by MS177, MS177N1 (which contains a moiety that does not bind CRBN; indicated by a cross-mark) and MS177N2 (which contains a moiety that does not bind EZH2). (b) A radioactive methyltransferase assay (3H-labeled S-Adenosyl methionine [SAM] as methyl donor) showing that MS177 exhibits a high inhibition potency for EZH2 and a high selectivity for EZH2 over EZH1. X-axis and y-axis show the used concentration of MS177 (in Log scale) and the rate of inhibition (treatment versus mock), respectively (n = 3; mean ± SD). IC50, half maximal inhibitory concentration. (c) Selectivity of MS177 (10 μM, relative to mock) against a panel of 23 different lysine, arginine or DNA methyltransferases in radioactive methyltransferase assays (n = 3; mean ± SD). (d) Immunoblotting of the indicated histone modification in Hela cells after a 24-hour treatment with different concentrations of C24, MS177, MS177N1 or MS177N2, in comparison to mock (DMSO). (e) Immunoblotting of PRC2 subunits (GAPDH as a loading control) and global H3K27 methylation levels (H3 as a loading control) in EOL-1 cells post-treatment with DMSO, the indicated concentrations of MS177, or 2.5 μM of C24, MS177N1 or MS177N2 for 16 hours. (f) Immunoblotting of PRC2 subunits (GAPDH as a loading control) in MV4;11 cells after a 24-hour treatment with the increasing concentration of MS177, relative to mock (DMSO). (g) Measurement of half-maximal degradation concentration (DC50) value of MS177 in MV4;11 cells, based on EZH2 immunoblotting signals in the MS177-treated and mock-treated cells (n = 2 independent experiments; mean ± SD; quantified with ImageJ).

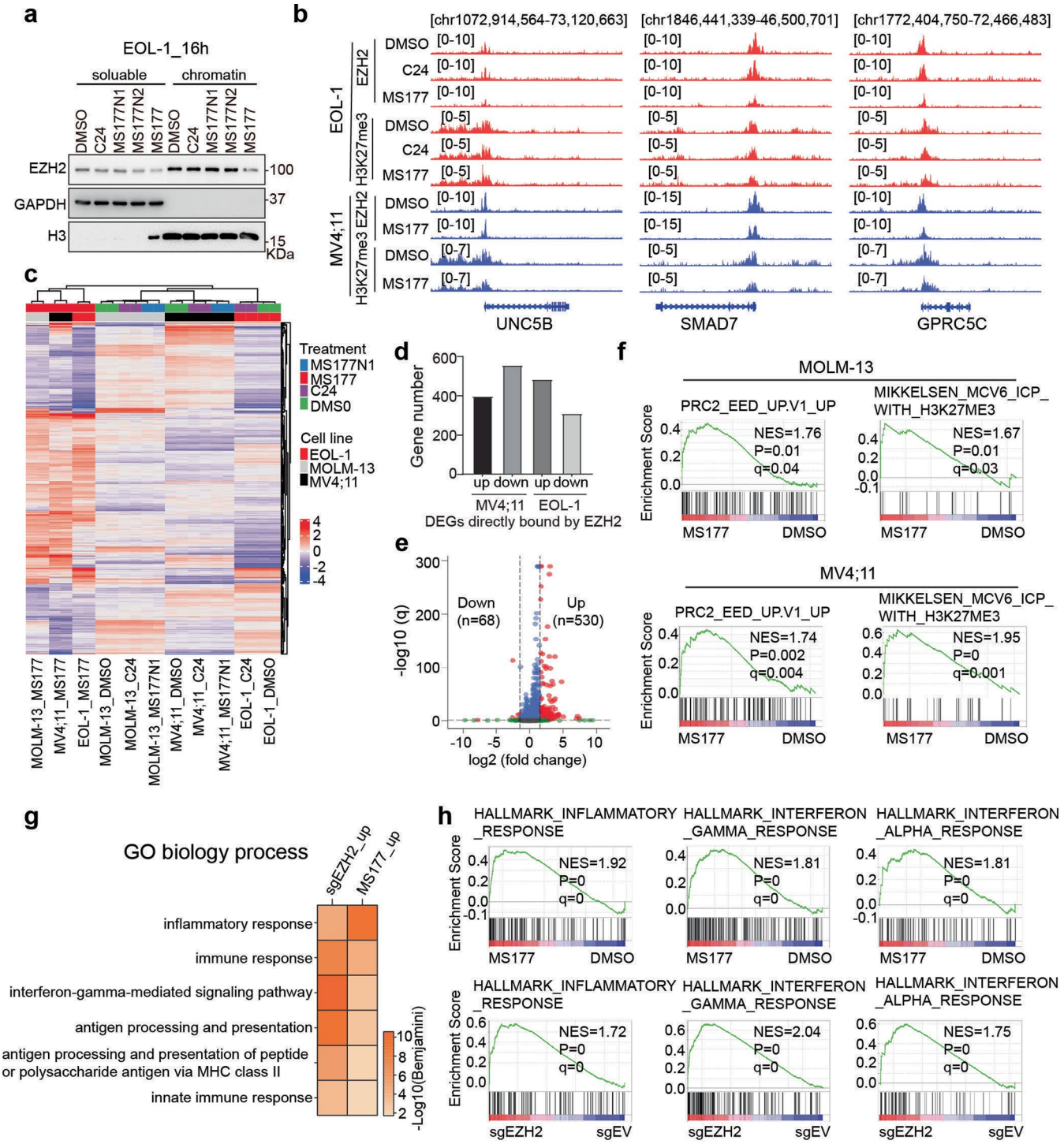

Extended Data Fig. 6 | See next page for caption.

Extended Data Fig. 6 | Integrated ChIP-seq and RNA-seq analysis showing the EZH2:PRC2 on-target effect of MS177. (a) Immunoblotting of EZH2, either nucleoplasmic (left) or chromatin-bound (right), in EOL-1 cells after a 16-hour treatment with DMSO or 2.5 μM of C24, MS177N1, MS177N2 or MS177. GAPDH and histone H3 serve as the cell fractionation controls. (b) IGV views of EZH2 and H3K27me3 ChIP-seq peaks at the indicated EZH2:PRC2 target gene post-treatment of EOL-1 (upper; for 16 hours) and MV4;11 cells (bottom; for 24 hours) with either DMSO or 0.5 μM of C24 or MS177. (c) Unsupervised clustering analysis using the RNA-seq-based transcriptome profiles of the three independent MLL-r acute leukaemia cell lines after the treatment with DMSO or 0.5 μM of MS177, C24 or MS177N1. MV4;11 and MOLM13 cells were treated for 24 hours, and EOL-1 cells for 16 hours (n = 2 replicated samples). (d) Bar plot showing the number of DEGs associated with the direct EZH2 binding in MV4;11 (left) or EOL-1 (right) cells. Up and down refer to those up- and down-regulated DEGs, respectively, based on RNA-seq analysis. (e) Volcano plot showing differential expression analysis of genes based on RNA-seq profiles of EOL-1 cells with EZH2 KO versus mock control (n = 2 replicated samples). The x-axis shows the log2 value of fold-change in gene expression (in KO versus vector-treated cells) and the y-axis shows the -log10 value of adjusted P (q) value, with the dashed lines indicating the cut-off of significance. (f) GSEA revealing that, relative to DMSO, MS177 treatment is positively correlated with upregulation of the indicated genes repressed by PRC2:EED (left) or bound by H3K27me3 (right) in MOLM-13 (top) or MV4;11 (bottom) cells. (g) DAVID functional annotation reveals that the DEGs up-regulated after EZH2 KO (sgEZH2_up) or MS177 treatment (MS177_up) in EOL-1 cells have similar enrichment for the immunity-related genes. (h) GSEA shows that, relative to their respective controls, both MS177 treatment (top) and EZH2 KO (bottom) in EOL-1 cells are positively correlated with upregulation of the indicated immunity-related genesets.

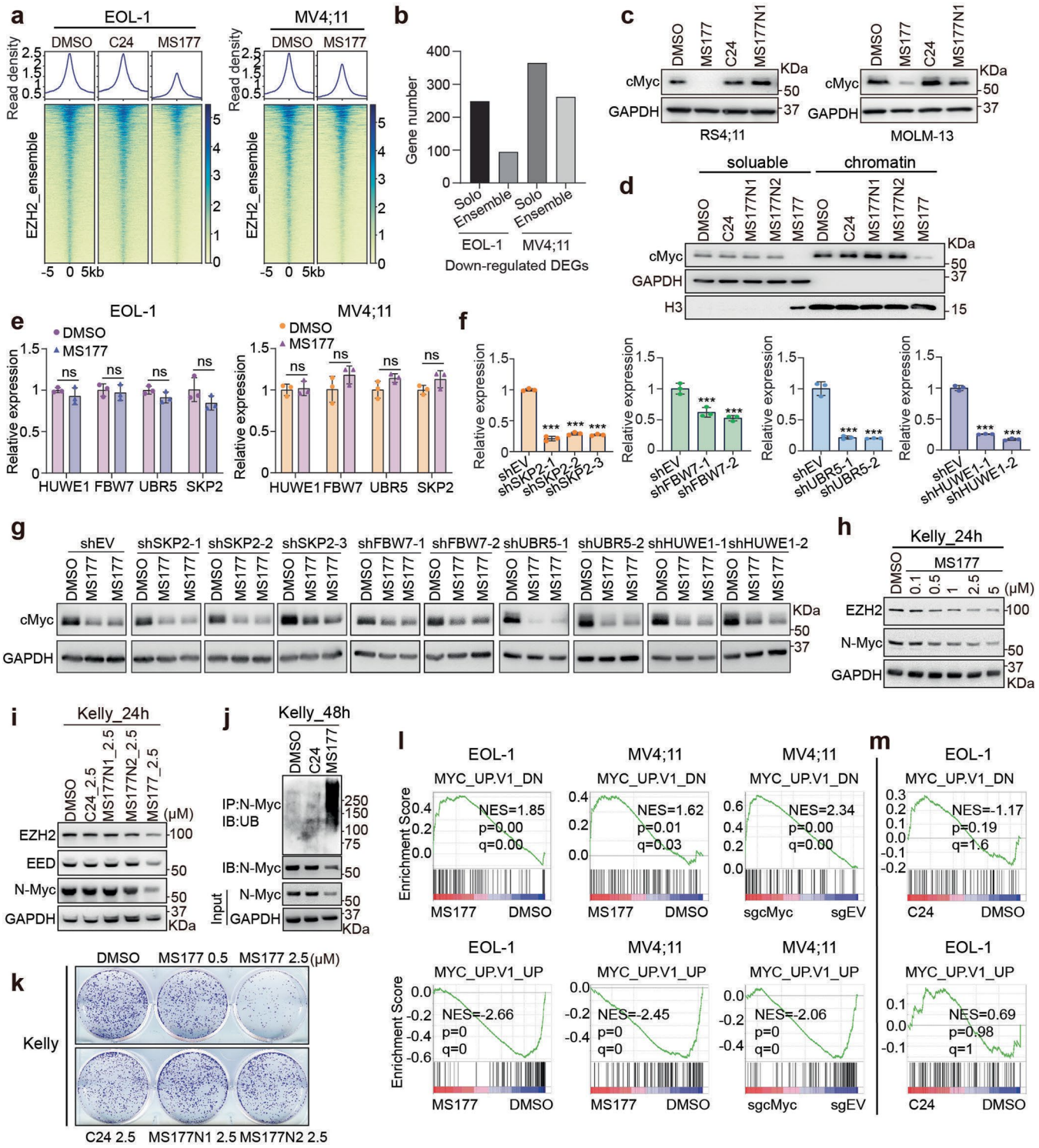

Extended Data Fig. 7 | See next page for caption.

Extended Data Fig. 7 | MS177 represses Myc-related oncogenic nodes by inducing Myc protein ubiquitination and degradation. (a) Heatmaps showing the EZH2 ChIP-seq signal intensities (normalized against spike-in control and sequencing depth) ± 5 kb around the centers of EZH2/H3K27me3-cobound 'ensemble' peaks in EOL-1 (left) and MV4;11 cells (right), treated for 16 and 24 hours respectively with DMSO (left), C24 (middle) or MS177 (right). (b) Bar plot showing the number of DEGs, down-regulated in EOL-1 (left) or MV4;11 (right) cells following the MS177 versus DMSO treatment, that displayed either the EZH2-'solo' or EZH2:PRC2 ('ensemble') binding. (c) Immunoblotting for cMyc in MLL-r leukemia cells treated with the indicated compound. (d) cMyc immunoblotting using the nucleoplasmic (left) and chromatin-bound (right) fractions of EOL-1 cells, treated with DMSO or 2.5 μM of C24, MS177N1, MS177N2 or MS177 for 16 hours. (e) RT-PCR for the indicated E3 ligase in EOL-1 and MV4;11 cells post-treatment with DMSO or 5 μM of MS177 for 4 hours (n = 3; mean ± SD; unpaired two-tailed Student's t-test). (f) RT-PCR for the indicated E3 ligase in MOLM-13 cells, stably expressed with an E3 ligase-targeting shRNAs or EV (n = 3; mean ± SD; unpaired two-tailed Student's t-test). (g) Immunoblotting for cMyc in MOLM-13 cells, stably expressed with an E3 ligase-targeting shRNA or EV, after the treatment with DMSO or 0.5 μM of MS177 for 24 hours. (h-i) Immunoblotting of EZH2, EED and N-Myc using lysate of Kelly cells after a 24-hour treatment with the increasing concentration of MS177 (h), in comparison to C24 and MS177's non-PROTAC analogs (i). (j) N-Myc ubiquitination immunoblotting in Kelly cells, treated for 48 hours with 2.5 μM of DMSO, C24 or MS177. (k) Colony formation of Kelly cells treated with the indicated compound. (l) GSEA revealing significant enrichments of the indicated cMyc-upregulated (up) or cMyc-repressed (down) genesets in the MS177-treated (left/middle) or cMyc-depleted (sgcMyc; right) cells. (m) GSEA revealing a lack of significant correlation between cMyc-regulated genes and C24 treatment in EOL-1 cells. *, **, and *** denote $P < 0.05$, 0.01 and 0.005, respectively. NS denotes not significant. Numerical source data, statistics, exact P values and unprocessed blots are available as source data.

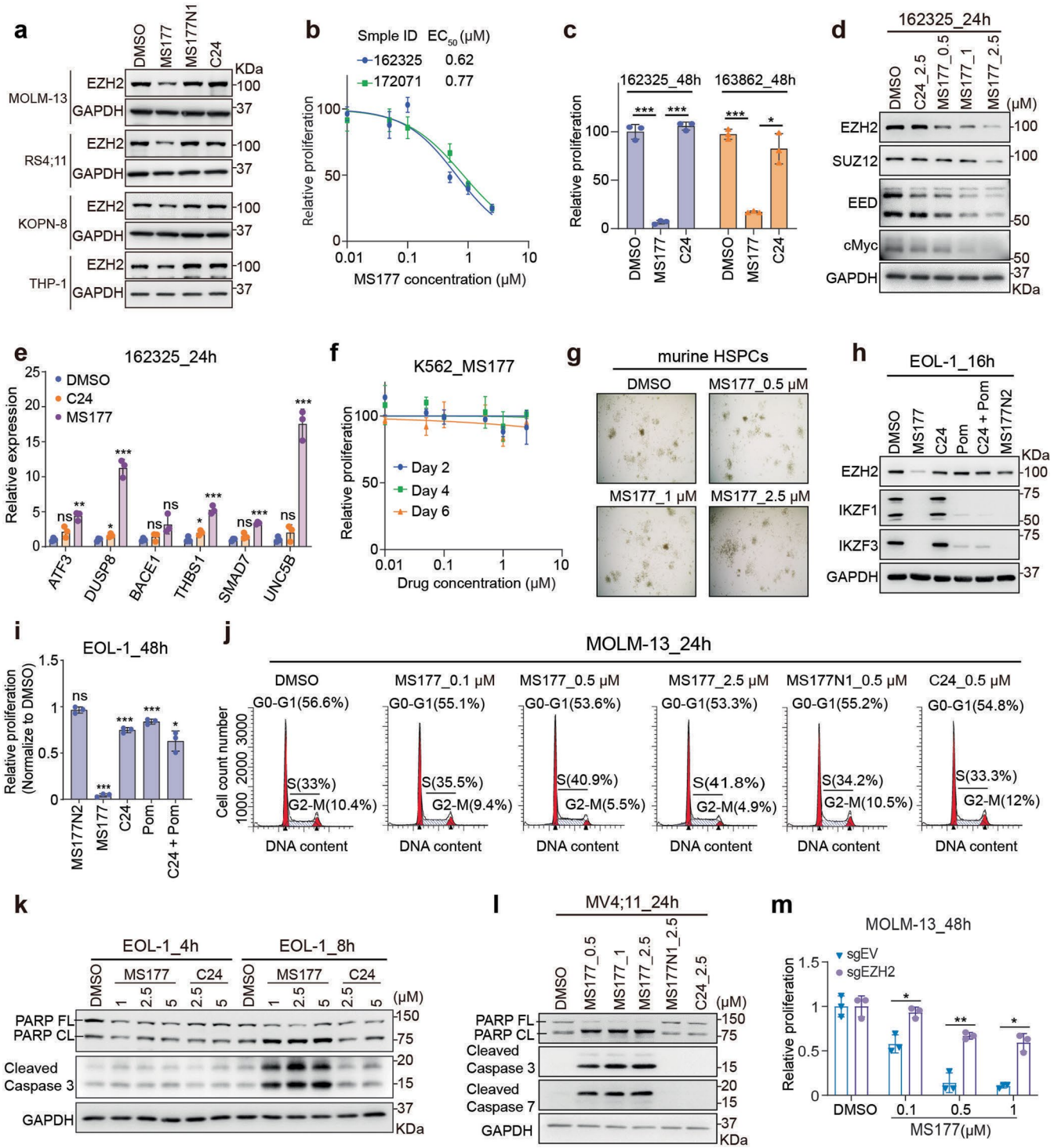

Extended Data Fig. 8 | See next page for caption.

Extended Data Fig. 8 | MS177 exhibits potent effect on inducing leukaemia cell growth inhibition, apoptosis, and cell cycle progression arrest. (a) Immunoblotting for EZH2 and GAPDH in four MLL-r leukaemia cell lines, treated with the indicated compound (0.5 μM) for 24 hours. (b) Effect of a 24-hour treatment with different concentrations of MS177 on proliferation of the two indicated primary samples from de-identified AML patients. Y-axis shows mean ± SD after normalization to DMSO-treated (n = 3). (c) Proliferation of primary AML cells treated with 1 μM of C24 or MS177, relative to DMSO, for 48 hours (n = 3; mean ± SD; unpaired two-tailed Student's t-test). (d-e) Immunoblotting for EZH2, PRC2 subunits and cMyc (d) and RT-qPCR for EZH2:H3K27me3-cobound genes (e) in primary AML cells, treated with the indicated compound (0.5 μM) for 24 hours. For e, y-axis shows RT-qPCR signals after normalization to those of GAPDH and to DMSO-treated cells (n = 3; mean ± SD; unpaired two-tailed Student's t-test). (f) Growth of K562 cells treated with MS177, relative to DMSO, for the indicated time. Y-axis shows mean ± SD after normalization to DMSO-treated (n = 3). (g) Representative view of colonies formed by murine HSPCs in the presence of DMSO or MS177. (h-i) Immunoblotting for EZH2 and IKZF1/3 (h) and growth (i) of EOL-1 cells after the indicated treatment of compound (0.5 μM for all). Pom, pomalidomide. For i, y-axis shows relative growth after normalization to DMSO-treated (n = 3; mean ± SD; unpaired two-tailed Student's t-test). (j) Representative flow cytometry-based histograms showing the DNA content in MOLM-13 cells, treated with indicated compound for 24 hours. (k-l) Immunoblotting for apoptotic markers in EOL-1 (k) or MV4;11 (l) cells after the indicated compound treatment. (m) Proliferation of the EZH2-depleted (sgEZH2) or control (sgEV) MOLM-13 cells, treated with DMSO or MS177 (0.1, 0.5 or 1 μM) for 48 hours (n = 3; mean ± SD; unpaired two-tailed Student's t-test). *, **, and *** denote the P value of < 0.05, 0.01 and 0.005, respectively. NS denotes not significant. Numerical source data, statistics, exact P values and unprocessed blots are available as source data.

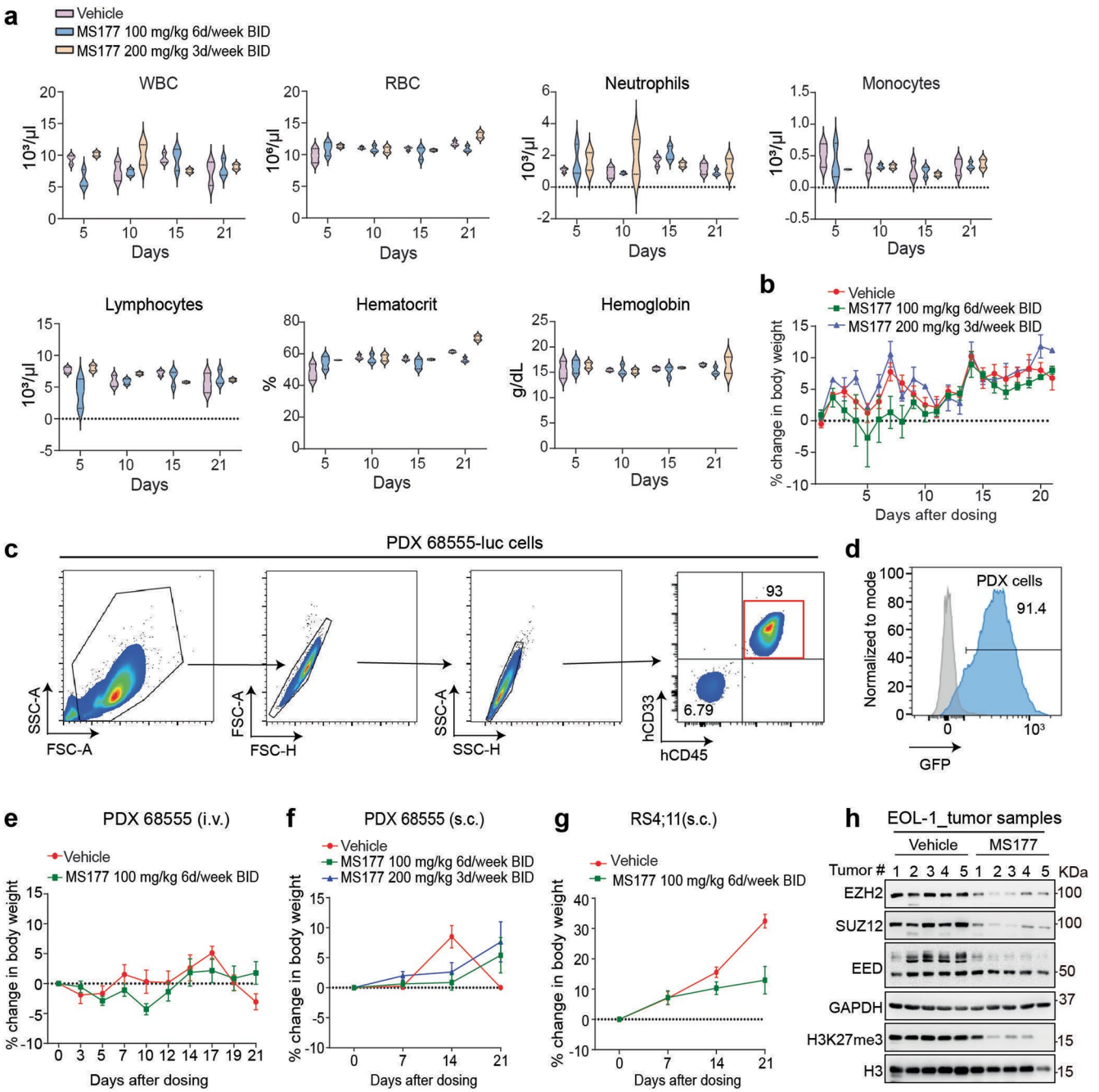

Extended Data Fig. 9 | MS177 represses MLL-r leukaemia growth in multiple animal models established by human cell line xenograft or PDX. (a) Violin plots showing complete blood counting (CBC) of white blood cells (WBC), red blood cells (RBC), neutrophils and lymphocytes, as well as hematocrit or hemoglobin, in C57BL/6 mice treated with either vehicle (n = 3) or MS177 (with a dose of 100 mg/kg, BID, 6 days/week, i.p. [n = 3]; or 200 mg/kg, BID, 3 days/week, i.p. [n = 2]) on day 5, 10, 15 and 21. The boundaries of the violin plots indicate the 25th and 75th percentiles. (b) The body weight change of C57BL/6 mice treated with either vehicle (n = 3; mean ± SD) or MS177 (100 mg/kg, BID, 6 days/week, i.p. [n = 3; mean ± SD]; or 200 mg/kg, BID, 3 days/week, i.p. [n = 2; mean ± SD]) over a course of 21 days. (c-d) Flow cytometry-based analysis for the expression of human-specific cell surface antigens (~93% as hCD45 + /hCD33 +, c) and GFP (from a cell-labeling construct, d) among the splenic cells harvested from leukemic mice, established by intravenous (i.v.) injection of an MLL-r AML PDX line carrying the stably expressed luciferase/GFP reporter (PDX # 68555-Luc). (e-f) Body weight change of NSG-SGM3 mice bearing the MLL-r AML PDX tumors, xenografted either intravenously (e) or subcutaneously (s.c.; f), as measured from the starting time point of treatment with the indicated dose of vehicle or MS177 over a course of 21 days. Mean ± SD. (g) Body weight change of NSG mice bearing the subcutaneous RS4;11 cell xenografts, as measured from the starting point of treatment with the indicated dose of vehicle or MS177 over a course of 21 days. Mean ± SD. (h) Immunoblotting for the indicated proteins using a collection of the s.c. xenografted EOL-1 tumors, which were freshly isolated from NSG mice treated with vehicle or 200 mg/kg of MS177 (BID per day) for a total of 5 days. Numerical source data and unprocessed blots are available as source data.

nature portfolio

Corresponding author(s): Gang Greg Wang, Jian Jin

Last updated by author(s): Jan 13, 2022

Reporting Summary

Nature Portfolio wishes to improve the reproducibility of the work that we publish. This form provides structure for consistency and transparency in reporting. For further information on Nature Portfolio policies, see our Editorial Policies and the Editorial Policy Checklist.

Statistics

For all statistical analyses, confirm that the following items are present in the figure legend, table legend, main text, or Methods section.

n/a	Confirmed
☐	☒ The exact sample size (*n*) for each experimental group/condition, given as a discrete number and unit of measurement
☐	☒ A statement on whether measurements were taken from distinct samples or whether the same sample was measured repeatedly
☐	☒ The statistical test(s) used AND whether they are one- or two-sided *Only common tests should be described solely by name; describe more complex techniques in the Methods section.*
☒	☐ A description of all covariates tested
☒	☐ A description of any assumptions or corrections, such as tests of normality and adjustment for multiple comparisons
☐	☒ A full description of the statistical parameters including central tendency (e.g. means) or other basic estimates (e.g. regression coefficient) AND variation (e.g. standard deviation) or associated estimates of uncertainty (e.g. confidence intervals)
☐	☒ For null hypothesis testing, the test statistic (e.g. *F*, *t*, *r*) with confidence intervals, effect sizes, degrees of freedom and *P* value noted *Give P values as exact values whenever suitable.*
☒	☐ For Bayesian analysis, information on the choice of priors and Markov chain Monte Carlo settings
☒	☐ For hierarchical and complex designs, identification of the appropriate level for tests and full reporting of outcomes
☒	☐ Estimates of effect sizes (e.g. Cohen's *d*, Pearson's *r*), indicating how they were calculated

Our web collection on statistics for biologists contains articles on many of the points above.

Software and code

Policy information about availability of computer code

Data collection	NextSeq System Suite v2.2.0, Attune'M NxT Software v2.7
Data analysis	For RNAseq data analysis: Fastq files were aligned to the GRCh38 human genome (GRCh38.d1.vd1.fa) using STAR v2.4.2 with the following parameters: --outSAMtype BAM Unsorted --quantMode TranscriptomeSAM. Transcript abundance for each sample was estimated with salmon v0.1.19 to quantify the transcriptome defined by Gencode v22. Raw read counts were used for differential gene expression analysis by DESeq2 v1.38.2.Volcano plots visualizing the DEGs were produced using R's package "EnhancedVolcano" v3.11 with the indicated filters. For ChIPseq data analysis: ChIP-seq reads were mapped to the human genome (hg19) and drosophila genome (dm3) using the BWA (V0.7.12; default parameters) alignment software. Samtools (vl.9), Picard MarkDuplicates funtion (v2.20.4), and bedtools (v2.28.0) were used to remove the non-primary alignment, PCR duplicates, or blacklist regions from aligned data. MACS2(v2.1.1) was used for peak calling. Deeptools (v3.3.0) was used to make bigwig files, heatmaps, and averaged plottings of ChIP-seq signal. These bigwig files were visualized using IGV v2.5.3. For CUT&RUN Data Analysis: CUT&RUN raw reads were mapped to the reference genome (hg19) using bowtie2.3.5. The non-primary alignment, PCR duplicates, or blacklist regions were removed from aligned data by Samtools (v1.9), Picard 'MarkDuplicates' function (v2.20.4), and bedtools (v2.28.0), respectively. Peak calling was performed using MACS2 (macs2 callpeak -f BAMPE -g hs/mm –keep-dup 1). Deeptools (v3.3.0) was used to generate bigwig files, heatmaps and averaged plotting of CUT&RUN signals. FACS data were analyzed by FlowJo 10.7.1. Cell cycle data was analysed by ModFit v5.0.

For manuscripts utilizing custom algorithms or software that are central to the research but not yet described in published literature, software must be made available to editors and reviewers. We strongly encourage code deposition in a community repository (e.g. GitHub). See the Nature Portfolio guidelines for submitting code & software for further information.

Data

Policy information about availability of data

All manuscripts must include a data availability statement. This statement should provide the following information, where applicable:

- Accession codes, unique identifiers, or web links for publicly available datasets
- A description of any restrictions on data availability
- For clinical datasets or third party data, please ensure that the statement adheres to our policy

Genomic data produced by this study, including ChIP-Seq, CUT&RUN and RNA-Seq, have been deposited in NCBI Gene Expression Omnibus (GEO) database under accession code GSE180448. The gene-expression data of primary human AML patient samples were derived from the TCGA Research Network: http://cancergenome.nih.gov/. Other publicly available genomic datasets used in this work included those under the NCBI GEO accession numbers GSE113042 (including ChIP-seq data of H3K4me3, H3K27ac, SMARCA4 and SMARCC1 in EOL-1 cells), GSE82116 (including ChIP-seq data of H3K27ac, H3K9ac and POL2 in MV4;11 cells), GSE73528 (including ChIP-seq data of MLLn and MLLc in MV4;11 cells), GSE101821 (including ChIP-seq data of BRD4 in MV4;11 cells), GSE29611 (including ChIP-seq data of EZH2 and H3K27me3 in GM12878, HUVEC and K562 cells as well as SUZ12 in K562 cells), GSE30226 (including ChIP-seq data of cMyc in HUVEC and K562 cells) and GSE33213 (including ChIP-seq data of cMyc in GM12878 cells). All other data supporting the findings of this study are available from the corresponding authors on reasonable request. Source data are provided with this paper.

Field-specific reporting

Please select the one below that is the best fit for your research. If you are not sure, read the appropriate sections before making your selection.

☒ Life sciences ☐ Behavioural & social sciences ☐ Ecological, evolutionary & environmental sciences

For a reference copy of the document with all sections, see nature.com/documents/nr-reporting-summary-flat.pdf

Life sciences study design

All studies must disclose on these points even when the disclosure is negative.

Sample size	No statistical measures were used to determine sample size. Sample sizes were estimated based on preliminary experiments and similar studies in the previously published data.
Data exclusions	No data was excluded from analysis
Replication	All experiments were reproduced reliably in independent setting for at least two or three times.
Randomization	All the samples used in the study were randomly allocated.
Blinding	Investigators were blinded to group allocation during data collection in the animal experiments. Blinded data analysis was carried out as well, except when data were analyzed by pre-defined, well-accepted cut-offs and not easily subjected to investigator bias. For in vivo study, the Core facility helped to randomly allocated the mice groups and tumor measurements and images taking were performed by the Core staff in a blinded manner.

Reporting for specific materials, systems and methods

We require information from authors about some types of materials, experimental systems and methods used in many studies. Here, indicate whether each material, system or method listed is relevant to your study. If you are not sure if a list item applies to your research, read the appropriate section before selecting a response.

Materials & experimental systems

n/a	Involved in the study
☐	☒ Antibodies
☐	☒ Eukaryotic cell lines
☒	☐ Palaeontology and archaeology
☐	☒ Animals and other organisms
☐	☒ Human research participants
☒	☐ Clinical data
☒	☐ Dual use research of concern

Methods

n/a	Involved in the study
☐	☒ ChIP-seq
☐	☒ Flow cytometry
☒	☐ MRI-based neuroimaging

Antibodies

Antibodies used	EZH2 mouse mAb, BD, Cat #612666, Clone 11, 1:1000 for WB; EED sheep polyclonal, R&D, Cat #AF5827, 1:500 for WB; SUZ12 rabbit polyclonal, Abcam, Cat #ab12073, 1:1000 for WB; Histone H3 (tri methyl K9) rabbit polyclonal, Abcam, Cat #ab8898, 1:2000 for WB;

Histone H3 (acetyl K27) rabbit polyclonal, Abcam, Cat #ab4729, 1:5000 for WB and 1:100 for CUT&RUN; Histone H3 (tri methyl K36) rabbit polyclonal, Abcam, Cat #ab9050, 1:2000 for WB; Histone H3 (tri methyl K79) rabbit polyclonal, Abcam, Cat #ab2621, 1:2000 for WB; Histone H4 (tri methyl K20) rabbit polyclonal, Abcam, Cat #ab9053, 1:2000 for WB; Histone H3 (acetyl K18) rabbit polyclonal, Abcam, Cat #ab1191, 1:5000 for WB; Histone H3 rabbit polyclonal, Abcam, Cat #ab1791, 1:10000 for WB; Histone H4ac antibody, Abcam, Cat #ab177790, 1:5000 for WB; Mouse Anti-cMyc monoclonal, Abcam, Cat #ab17355, Clone 11, 1:2500 for WB; Rabbit Anti-cMyc monoclonal, Abcam, Cat #ab32072, clone Y69, 1:100 for CUT&RUN; Rabbit Anti-RNA polymerase II CTD repeat YSPTSPS (phospho S5) polyclonal, Abcam, Cat #ab5131, 1:1000 for WB; Rabbit Anti-ARID1A (BAF250a), Abcam, Cat #182560, 1:1000 for WB; Rabbit Anti-BRG1 (SMARCA4), Abcam, Cat #110641, 1:1000 for WB; Histone H3K4me3 rabbit polyclonal, Active Motif, Cat #39159, 1:5000 for WB; Ubiquitin (P4D1) mouse monoclonal, Santa Cruz Biotechnology, Cat #SC-8017, clone P4D1, 1:1000 for WB; HA tag rabbit mAb, Cell Signaling Technology, Cat #3724, clone C29F4, 1:5000 for WB, 1:100 for CUT&RUN; EZH2 rabbit mAb, Cell Signaling Technology, Cat #5246, clone D2C9, 1:50 for ChIP-seq and 1:100 for CUT&RUN; Normal Rabbit IgG, Cell Signaling Technology, Cat #2729, 1:100 for CUT&RUN; Rabbit Anti-DYKDDDDK Tag Polyclonal Antibody, Cell Signaling Technology, Cat #14793, 1:5000 for WB; Rabbit anti-Cleaved Caspase-3, Cell Signaling Technology, Cat #9661, 1:1000 for WB; Cleaved Caspase-7 rabbit mAb, Cell Signaling Technology, Cat #8438, clone D6H1, 1:1000 for WB; PARP rabbit mAb, Cell Signaling Technology, Cat #9532, clone 46D11, 1:1000 for WB; α-Tubulin rabbit mAb, Cell Signaling Technology, Cat #3873, clone DM1A, 1:5000 for WB;GAPDH rabbit mAb, Cell Signaling Technology, Cat #5174, clone D16H11, 1:5000 for WB; cMyc rabbit mAb, Cell Signaling Technology, Cat # 5605, clone D84C12, 1:1000 for WB and 1:100 for CUT&RUN; MAX rabbit mAb, Cell Signaling Technology, Cat #4739, clone S20, 1:1000 for WB; N-Myc rabbit mAb, Cell Signaling Technology, Cat #84406, clone D1V2A, 1:1000 for WB; CRBN rabbit mAb, Cell Signaling Technology, Cat #71810, clone D8H3S, 1:1000 for WB; Mono-Methyl-Histone H3 (Lys27) rabbit mAb, Cell Signaling Technology, Cat #84932, clone D3R8N, 1:5000 for WB; Di-Methyl-Histone H3 (Lys27) rabbit mAb, Cell Signaling Technology, Cat #9728, clone D18C8, 1:5000 for WB; Tri-Methyl-Histone H3 (Lys27) rabbit mAb, Cell Signaling Technology, Cat #9733, clone C36B11, 1:5000 for WB, 1:100 for ChIP-seq and 1:50 for CUT&RUN; Ikaros (IKZF1) Rabbit mAb, Cell Signaling Technology, Cat #14859, clone D6N9Y, 1:1000 for WB; Ikaros (IKZF3) Rabbit mAb, Cell Signaling Technology, Cat #15103, clone D1C1E, 1:1000 for WB; SMARCB1/BAF47 Rabbit mAb, Cell Signaling Technology, Cat #91735, clone D8M1X, 1:1000 for WB; Histone H2Av antibody rabbit polyclonal, Active Motif, Cat #39715, 1:100 for ChIP-seq; Anti-mouse IgG, HRP-linked Antibody, Cell Signaling Technology, Cat #7076, 1:5000 for WB; Anti-rabbit IgG, HRP-linked Antibody, Cell Signaling Technology, Cat #7074, 1:5000 for WB; Sheep IgG HRP-conjugated Antibody, R&D, Cat # HAF016, 1:2500 for WB; Anti-FLAG M2-HRP Monoclonal Antibody, Sigma, Cat #A8592, 1:5000 for WB; His-tag mouse monoclonal, Proteintech, Cat #66005-1, Clone 1B7G5, 1:2500 for WB; APC Mouse Anti-Human CD33,BD Biosciences, Cat #561817, 1:100 for flow; PE Mouse Anti-Human CD45, BD Biosciences, Cat #561866, 1:100 for flow.

Validation

All the antibodies used were validated by the manufactures and the validating data was provided on their websites. Furthermore, we also used positive and negative controls to further validate the antibody specificity by western blotting. For histone antibodies, specificity was also extensively examined by many independent investigators in addition to the vendor (refer to http://www.histoneantibodies.com/).

Eukaryotic cell lines

Policy information about cell lines

Cell line source(s)

Cell lines used in the study included HEK293T (ATCC, CRL-3216), HS27 cells (ATCC, CRL-1634), and Hela cells (ATCC, CCL-2). Human hematological cancer cell lines used in the study include K562 (ATCC, CRL-243), MV4;11 (ATCC, CRL-9591), RS4;11 (ATCC, CRL-1873), MOLM-13 (DSMZ, ACC554), KOPN-8 (DSMZ, ACC552), EOL-1 (DSMZ, ACC386), and THP-1 (ATCC, TIB-202). MM1.S(CRBN-/-), an MM1.S derivative line with knockout (KO) of the E3 ligase CRBN, was a kind gift of Drs. J Brander and W Kaelin (DFCI).

Authentication

Authentication of cell line identities, including parental and their derived lines, was ensured by the Tissue Culture Facility (TCF) affiliated to UNC Lineberger Comprehensive Cancer Center with the genetic signature profiling and fingerprinting analysis.

Mycoplasma contamination

Cell line was negativly tested for mycoplasm. Every month, a routine examination of cell lines in culture for any possible mycoplasma contamination was performed using commercially available detection kits (Lonza).

Commonly misidentified lines
(See ICLAC register)

No commonly misidentified lines were used in this study

Animals and other organisms

Policy information about studies involving animals; ARRIVE guidelines recommended for reporting animal research

Laboratory animals

NOD-SCID IL2Rgnull-3/GM/SF mice (NSG-SGM3), NOD/SCID/IL2Rgamma-null (NSG), or normal mice (C57BL/6 strain) were purchased from Jackson Lab and maintained by Animal Studies Core of the UNC Lineberger Comprehensive Cancer Center. All mice used in the study were female with an age of 8 weeks.

Wild animals

No wild animals were used in this study

Field-collected samples

No field-collected samples were used in this study

Ethics oversight

All animal experiments are approved by and performed in accord with the guidelines of the Institutional Animal Care and Use Committee (IACUC) at UNC.

Note that full information on the approval of the study protocol must also be provided in the manuscript.

Human research participants

Policy information about studies involving human research participants

Population characteristics	This study did not involve recruitment of patients or usage of clinical data. Patient-derived cells from the UNC Tissue Procurement Facility (TPF) or Public Repository of Xenografts (PRoXe; www.proxe.org) were used in this study for the in vitro drug treatment study and in vivo study, respectively. The detailed information for these patient samples were included in the Supplementary Table 8. No demographic identifiers were obtained for any of the de-identified patients.
Recruitment	No patients were recruited.
Ethics oversight	De-identified human samples and informed consent were obtained from the patients by the UNC Tissue Procurement Facility (TPF) under the protocol (UNC-LCCC-9001). This current study did not involve recruitment of patients or usage of clinical data. No participant compensation was provided in this study. No demographic identifiers were obtained for any of the patients. Cryopreserved specimen of an MLL-AF9+ AML Patient-derived Xenograft (PDX) model was obtained from Public Repository of Xenografts (DFAM-68555, PRoXe; www.proxe.org).

Note that full information on the approval of the study protocol must also be provided in the manuscript.

ChIP-seq

Data deposition

☒ Confirm that both raw and final processed data have been deposited in a public database such as GEO.

☒ Confirm that you have deposited or provided access to graph files (e.g. BED files) for the called peaks.

Data access links *May remain private before publication.*	https://www.ncbi.nlm.nih.gov/geo/query/acc.cgi?acc=GSE180448
Files in database submission	EOL1_DMSO_INPUT1_S4_R1_001.fastq.gz EOL1_DMSO_H3K27ME3PLUSH2AV_S1_R1_001.fastq.gz EOL1_C24_H3K27ME3PLUSH2AV_S2_R1_001.fastq.gz EOL1_177A_H3K27ME3PLUSH2AV_S3_R1_001.fastq.gz MV4-11_DMSO_H3K27me3_plus_H2Av_input_S6_R1_001.fastq.gz MV4-11_DMSO_H3K27me3_plus_H2Av_S3_R1_001.fastq.gz MV4-11_177A_H3K27me3_plus_H2Av_S5_R1_001.fastq.gzD_EZH2_input_S4_R1_001.fastq.gz EOL_D_EZH2_S1_R1_001.fastq.gz EOL_C24_EZH2_S2_R1_001.fastq.gz EOL_177_EZH2_S3_R1_001.fastq.gz MV_D_EZH2_input_S8_R1_001.fastq.gz MV_D_EZH2_S5_R1_001.fastq.gz MV_177_EZH2_S7_R1_001.fastq.gz EOL1_DMSO_H3K27me3_ChIP_with_spikein.bw EOL1_C24_H3K27me3_ChIP_with_spikein.bw EOL1_MS177_H3K27me3_ChIP_with_spikein.bw MV4-11_DMSO_H3K27me3_ChIP_with_spikein.bw MV4-11_MS177_H3K27me3_ChIP_with_spikein.bw EOL1_DMSO_EZH2_ChIP_with_spikein.bw EOL1_C24_EZH2_ChIP_with_spikein.bw EOL1_MS177_EZH2_ChIP_with_spikein.bw MV4-11_DMSO_EZH2_ChIP_with_spikein.bw MV4-11_MS177_EZH2_ChIP_with_spikein.bw EOL_HA-EZH2_R1/R2_001.fastq.gz EOL_MYC_CST_R1/R2.fastq.gz EOL1_MYC_AB_R1/R2_001.fastq.gz MV_HA-EZH2_R1/R2_001.fastq.gz MV_MYC_CST_R1/R2.fastq.gz MV4_MYC_AB_R1/R2_001.fastq.gz PDX_EZH2_R1/R2_001.fastq.gz PDX_H3K27ME3_R1/R2.fastq.gz PDX_MYC_R1/R2_001.fastq.gz PDX_H3K27AC_R1/R2_001.fastq.gz EOL_HA-EZH2_ext250_RPGC.bw EOL_MYC_CST_ext250_RPGC EOL_MYC_AB_ext250_RPGC.bw MV_HA-EZH2_ext250_RPGC.bw MV4_MYC_CST_ext250_RPGC MV_MYC_AB_ext250_RPGC.bw PDX_EZH2_ext250_RPGC.bw PDX_H3K27ME3_ext250_RPGC.bw PDX_MYC_ext250_RPGC.bw PDX_H3K27AC_ext250_RPGC.bw

Genome browser session (e.g. UCSC)	We only deposit data on GEO and not at the Genome browser.

Methodology

Replicates	Multiple MLL-rearranged leukemia models were used including EOL-1 cells (harboring MLL-PTD), MV4;11 cells (harboring MLL-AF4 fusion) and a human AML PDX model harboring MLL-AF9. And independent profiling approaches were used for genomic mapping studies. Specifically, two different anti-cMyc antibodies were used for cMyc CUT&RUN; and two different antibodies and approaches were used for EZH2 binding profiling (i.e. EZH2 ChIP-seq and HA-EZH2 CUT&RUN).
Sequencing depth	EOL1_DMSO_INPUT1_S4_R1_001.fastq.gz single-end 50 EOL1_DMSO_H3K27ME3PLUSH2AV_S1_R1_001.fastq.gz single-end 50 EOL1_C24_H3K27ME3PLUSH2AV_S2_R1_001.fastq.gz single-end 50 EOL1_177A_H3K27ME3PLUSH2AV_S3_R1_001.fastq.gz single-end 50 MV4-11_DMSO_H3K27me3_plus_H2Av_input_S6_R1_001.fastq.gz single-end 50 MV4-11_DMSO_H3K27me3_plus_H2Av_S3_R1_001.fastq.gz single-end 50 MV4-11_177A_H3K27me3_plus_H2Av_S5_R1_001.fastq.gz single-end 50 EOL_D_EZH2_input_S4_R1_001.fastq.gz single-end 50 EOL_D_EZH2_S1_R1_001.fastq.gz single-end 50 EOL_C24_EZH2_S2_R1_001.fastq.gz single-end 50 EOL_177_EZH2_S3_R1_001.fastq.gz single-end 50 MV_D_EZH2_input_S8_R1_001.fastq.gz single-end 50 MV_D_EZH2_S5_R1_001.fastq.gz single-end 50 MV_177_EZH2_S7_R1_001.fastq.gz single-end 50 EOL_HA-EZH2_R1/R2_001.fastq.gz pair-end 75 EOL_MYC_CST_R1/R2.fastq.gz pair-end 75 EOL1_MYC_AB_R1/R2_001.fastq.gz pair-end 75 MV_HA-EZH2_R1/R2_001.fastq.gz pair-end 75 MV_MYC_CST_R1/R2.fastq.gz pair-end 75 MV4_MYC_AB_R1/R2_001.fastq.gz pair-end 75 PDX_EZH2_R1/R2_001.fastq.gz pair-end 75 PDX_H3K27ME3_R1/R2.fastq.gz pair-end 75 PDX_MYC_R1/R2_001.fastq.gz pair-end 75 PDX_H3K27AC_R1/R2_001.fastq.gz pair-end 75
Antibodies	anti-EZH2, Cell Signaling Technology, Cat #5246; anti-H3K27me3, Cell Signaling Technology, Cat #9733; anti-H2Av (for Drosophila spike-in chromatin), Active Motif, Cat #39715; anti-HA, Cell Signaling Technology, Cat # 3724; anti-cMyc, Cell Signaling Technology, Cat # 3873; anti-cMyc, Abcam, Cat # ab32072; anti-H3K27ac, Abcam, Cat # ab4729;
Peak calling parameters	MACS2 with the parameter: --nomodel --pvalue 1e-05 --extsize 250
Data quality	FastQC
Software	STAR (v2.7.1a), DeepTools(v3.3.0), MACS(v2.1.1)

Flow Cytometry

Plots

Confirm that:

☒ The axis labels state the marker and fluorochrome used (e.g. CD4-FITC).

☒ The axis scales are clearly visible. Include numbers along axes only for bottom left plot of group (a 'group' is an analysis of identical markers).

☒ All plots are contour plots with outliers or pseudocolor plots.

☒ A numerical value for number of cells or percentage (with statistics) is provided.

Methodology

Sample preparation	For antibody staining: cells were washed once in the cold FACS buffer (PBS with 5% of FBS added), then resuspended to a final density of 1 million cells per ml in the FACS buffer, and incubated with the added respective antibodies (1:100 dilution) for 30 minutes on ice. Then, cell pellet was collected and washed with the FACS buffer. Finally, the stained cells were subject to analysis with the FACS machine. For cell cycle analysis: cells were collected, washed with ice-cold PBS and fixed in pre-chilled methanol (80%), followed by staining with PBS plus 20 µg/mL of propidium iodide (Sigma), 0.1% of Triton-X100 and 200 µg/mL of RNase A (Roche), followed by flow cytometry analysis.

Instrument	Attune Nxt (Life Technologies), CyAnADP flow cytometer (Beckman-Coulter)
Software	Data were collected and analyzed using the FlowJo and ModFit software.
Cell population abundance	For cell cycle analysis, cell populations were composed of cancer cells and all cells were used for analysis. For sorting, cells isolated from mice were labeled with human-specific cell surface antigen antibody and the purity of cells after sorting was over 93%.
Gating strategy	Cells without antibody staining were used to set the gating for analysis.

☒ Tick this box to confirm that a figure exemplifying the gating strategy is provided in the Supplementary Information.